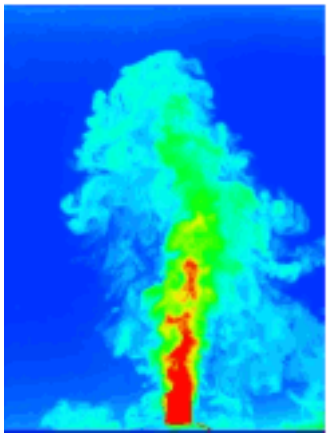

Journal of Turbulence
Publication details, including instructions for authors and subscription information:
http://www.tandfonline.com/loi/tjot20

On the performance of relaxation filtering for large-eddy simulation

D. Fauconnier [a], C. Bogey [b] & E. Dick [a]

[a] Department of Flow, Heat and Combustion Mechanics, Ghent University, St. Pietersnieuwstraat 41, B-9000 Ghent, Belgium

[b] Laboratoire de Mécanique des Fluides et d'Acoustique, UMR CNRS 5509, Ecole Centrale de Lyon, Université de Lyon, Ecully Cedex, 69134, France

To cite this article: D. Fauconnier , C. Bogey & E. Dick (2013): On the performance of relaxation filtering for large-eddy simulation, Journal of Turbulence, 14:1, 22-49

To link to this article: http://dx.doi.org/10.1080/14685248.2012.740567

Journal of Turbulence, 2013
Vol. 14, No. 1, 22–49, http://dx.doi.org/14685248.2012.740567

On the performance of relaxation filtering for large-eddy simulation

D. Fauconnier[a]*, C. Bogey[b] and E. Dick[a]

[a]*Department of Flow, Heat and Combustion Mechanics, Ghent University, St. Pietersnieuwstraat 41, B-9000 Ghent, Belgium;* [b]*Laboratoire de Mécanique des Fluides et d'Acoustique, UMR CNRS 5509, Ecole Centrale de Lyon, Université de Lyon, 69134 Ecully Cedex, France*

(*Received 16 April 2012; final version received 11 October 2012*)

In this work, the performance of large-eddy simulation (LES) based on the relaxation-filtering (RF) technique has been investigated quantitatively. In RF-based LES, the velocity field is filtered each nth time step, using a standard finite-difference filter, characterized by a specific order of accuracy m, and a fixed filtering strength σ. Hence, the procedure dissipates the amount of energy related to the residual stresses, and thus models the dissipative effect of the unresolved scales on the resolved scales. Since the order m and strength σ are related to the spectral distribution and the magnitude of the dissipation, respectively, these predefined parameters are crucial for the success of the method. Here, their influence is systematically investigated for the Taylor–Green vortex flow at a Reynolds number of 3000. First, the effects of m and σ are studied *a priori* in Fourier space. Further, 36 LESs are performed, each with a different combination of order $m = 4, 6, 8, 10, 12, 14$ and strength $\sigma = 0.15, 0.2, 0.4, 0.6, 0.8, 1$, and the turbulent statistics are compared with those of a direct numerical simulation, filtered at identical resolutions. The *a priori*, as well as the *a posteriori* results indicate that, for low filter orders $m \leq 4$, the LES accuracy is rather poor and depends strongly on the filtering strength σ. However, for higher order filters, i.e. $m \geq 8$, the accuracy is quite good and the results, including the resolved and subgrid dissipation rates, are nearly independent of the strength σ for $\sigma \geq 0.4$. In this case, the spectral dissipation-distribution, determined by m, turns out to be the dominant parameter, whereas the dissipation strength, determined by σ, is of minor importance.

Keywords: large-eddy simulation; subgrid modeling; relaxation filtering; error landscapes; Taylor–Green vortex

1. Introduction

In large-eddy simulation (LES) of a turbulent flow, the most significant scales of motion, i.e., the largest and most significant scales in the energy-containing range and inertial range, are resolved in order to obtain a statistically sufficiently accurate prediction of the flow. Since the small scales in the dissipation range are not resolved, their effects must be accounted for by a dissipation mechanism, in order to avoid pile-up of energy at the cutoff wavenumber imposed by the computational grid. This is usually done by replacing the residual stress tensor in the filtered Navier–Stokes equations with an eddy-viscosity model, such as the well-known Smagorinsky model, or by relying on the numerical dissipation induced by some specific discretization schemes of the convective term as in implicit LES methods. For a more detailed survey of these models, we refer to books by Sagaut [1] and Geurts [2], or reviews by Lesieur and Métais [3], Grinstein and Fureby [4], and

*Corresponding author. Email: dieter.fauconnier@ugent.be

Domaradzki [5]. Domaradzki et al. [6–8] and Bogey and Bailly [9,10] pointed out that the global amount of dissipation, as well as its spectral distribution, may be difficult to control in these methods. This has led to the development of other LES methodologies relying on high-order dissipation mechanisms, such as hyper-viscosity models [11,12], the relaxation term in the approximate deconvolution model (ADM) [13], or spectral-like/selective spatial filters [14].

In recent years, relaxation filtering (RF) has been proposed by Visbal and Rizzetta [15], Rizzetta et al. [16], Mathew et al. [17], and Bogey et al. [18–20], among others, as a novel technique to account for the dissipative effect of the residual stresses in LES. It is interesting to note that the RF method as described by Mathew et al. [17] is actually inspired on the ADM of Stolz, Adams, and Kleiser [13], who already suggested the use of explicit RF. In RF-based LES, the velocity field is filtered every n^{th} time step and in each Cartesian direction, using a standard finite-difference filter, characterized by a specific order of accuracy m, and a fixed filtering strength $\sigma \in [0, 1]$. Such a procedure is very successful in dissipating the energy related to the residual stresses, and thus models the dissipative effect of the unresolved scales on the resolved scales. To obtain the appropriate amount of energy dissipation, criteria were developed to adjust dynamically the filtering frequency and strength σ to the flow features, e.g., in Tantikul and Domaradzki [21].

However, since such dynamic procedures are often cumbersome and computationally expensive, the filtering is usually applied at a fixed frequency, using a predefined finite difference filter with order m, and filtering strength σ (typically $\sigma \simeq 1$). Since, the order m and strength σ determine the spectral distribution and the global magnitude of the dissipation, respectively, these predefined parameters are crucial for the success of the method. Indeed, it can be understood that the selected filter must provide sufficient dissipation to the smallest resolved scales, leaving the largest scales mostly unaffected. Hence, the influence of the spectral distribution, determined by the order m, is expected to be most important, whereas the influence of the filtering strength σ should be less important. Because of this we expect that the amount of energy, dissipated by the relaxation filter, should not depend significantly on the precise value of σ. This hypothesis is supported by the results of Bogey and Bailly [10,18] in LES of turbulent jets. They noticed that the dissipation rates did not change significantly when decreasing the relaxation filter frequency. The latter is equivalent to reducing σ for a fixed filtering frequency. Nevertheless, a systematic quantitative assessment of the RF approach, and in particular the influence of σ, is necessary, as pointed out in recent work of Berland et al. [22].

In this paper, we investigate in detail the performance of the RF method, using standard finite difference filters with adjustable strength, as modeling-approach for LES. As a representative test case, the Taylor–Green vortex flow is selected. The viscous Taylor–Green vortex flow, introduced in 1937 by Taylor et al. [23], is considered as a prototype system that describes the production of small-scale eddies due to the mechanism of vortex-line stretching in homogeneous isotropic turbulence [24]. It is one of the simplest environments to study the breakdown process of large-scale vortices into successively smaller ones, and the resulting homogeneous isotropic turbulence [24,25]. In the past decade, the Taylor–Green vortex has become a popular reference case, used in a series of studies on LES methods, e.g., by Fauconnier et al. [25], Drikakis et al. [26], Chandy and Frankel [27], Johnsen et al. [28], Adams [29], and Gassner and Beck [30]. We select the Reynolds number $\mathrm{Re} = 3000$, which is large enough so that natural transition into small-scale homogeneous isotropic decaying turbulence occurs.

The paper is organized as follows. After a brief introduction concerning the Taylor–Green vortex case at Reynolds $\mathrm{Re} = 3000$, the setup for the direct numerical simulation

(DNS) of this case is specified. The reference solution, obtained via DNS on a 384^3 computational grid, is presented and compared to the DNS results on a 256^3 grid and to the DNS data of Brachet et al. [24]. Further, the RF method for LES is introduced, followed by the setup for the parametric study in which the filter order m and the filter strength σ are the parameters of interest. More specific, the parametric study involves 36 RF-based LESs of the Taylor–Green vortex, each one performed on a 64^3 computational grid, using various combinations of standard filters of order m and filtering strength σ. For the quality assessment of the RF method for LES, the 36 LES datasets are compared with the filtered DNS reference data. We analyze the instantaneous energy spectra as well as the time evolutions of the kinetic energy and dissipation rate. The latter are determined based on LES and DNS data, filtered in post-processing to an effective resolution of 64^3, 32^3, and 16^3 nodes. This allows to isolate the effects of the RF on a large scale subset of the original data. In order to analyze and visualize the dependency and sensitivity of the RF method to both parameters, the deviation between the LES and DNS solutions, filtered at identical resolution, are presented as function of the filtering order m and strength σ in an error-landscape, following, e.g., Meyers et al. [31]. More importantly, we aim to validate the *a priori* expectations that the results should not vary significantly provided that the order of the relaxation filter is sufficiently high, and the strength is not unreasonably low.

2. Taylor–Green vortex

According to Brachet et al. [24], the generalized Taylor–Green vortex is defined as the periodic three-dimensional incompressible flow, governed by the Navier–Stokes equations and the continuity equation

$$\frac{\partial u_i}{\partial x_i} = 0, \tag{1}$$

$$\frac{\partial u_i}{\partial t} + u_j \frac{\partial u_i}{\partial x_j} = -\frac{\partial p}{\partial x_i} + \nu \frac{\partial^2 u_i}{\partial x_j^2}, \tag{2}$$

which develops from the initial solenoidal velocity field $\mathbf{u}(\mathbf{x}, t = 0)$ (in non-dimensional form)

$$\begin{aligned} u_1(\mathbf{x}, 0) &= \sin(x_1)\cos(x_2)\cos(x_3), \\ u_2(\mathbf{x}, 0) &= -\cos(x_1)\sin(x_2)\cos(x_3), \\ u_3(\mathbf{x}, 0) &= 0. \end{aligned} \tag{3}$$

The initial pressure field $p(\mathbf{x}, t = 0)$, that follows from the initial solenoidal velocity field, is obtained by solving the Poisson equation, yielding

$$p(\mathbf{x}, 0) = p_0 + \frac{1}{16}[2 + \cos(2x_3)][\cos(2x_1) + \cos(2x_2)], \tag{4}$$

where the arbitrary mean pressure component p_0 is set to zero in this work.

By taking the Fourier transform of the initial velocity field (3), it can be shown that the initial condition (3) corresponds to eight Fourier modes, located at the positions

$\boldsymbol{\kappa} = (\pm 1, \pm 1, \pm 1)$. Hence, condition (3) represents a single vortex scale which is located at the spherical wavenumber-shell with radius $|\kappa| = \sqrt{3}$. The total amount of kinetic energy and dissipation rate in the initial flow are obtained as

$$k\,(t=0) = \frac{1}{8\pi^3}\iiint_{\mathbf{0}}^{\mathbf{2\pi}} \frac{1}{2} u_i u_i d\mathbf{x} = \frac{1}{8}, \tag{5}$$

$$\varepsilon\,(t=0) = \frac{1}{8\pi^3}\iiint_{\mathbf{0}}^{\mathbf{2\pi}} \nu \frac{\partial u_i}{\partial x_j}\frac{\partial u_i}{\partial x_j} d\mathbf{x} = \frac{3}{4}\frac{1}{\mathrm{Re}}. \tag{6}$$

Brachet et al. [24] defined the Reynolds number as $\mathrm{Re} = 1/\nu$, noting that the length and velocity scales of the initial flow (3) are of order 1. In the initial stages of the simulation, the large-scale vortex flow is highly organized and, thus, characterized as laminar. However, the convective terms in the Navier–Stokes equations (2) start to generate successively smaller structures which interact with the large scales. If the Reynolds number is large enough, this results into a process of vortex-stretching and eventually into breakdown of the large scales into smaller ones which is interpreted as turbulence. Therefore, the Taylor–Green flow is believed to describe the fundamental process of natural transition into isotropic turbulence. This transitional behavior is determined entirely by the choice of the Reynolds number. Brachet et al. [24] observed that for $\mathrm{Re} \geq 500$ the small-scale structures in the Taylor–Green flow undergo profound changes. For high Reynolds numbers, say $\mathrm{Re} \geq 1000$, the *turbulent* flow becomes nearly isotropic with no memory of the initial conditions. Once $\mathrm{Re} \geq 1000$, an inertial range is observed in the energy spectrum. For $t \to \infty$, the isotropic turbulence decays due to viscosity.

We select the Reynolds number $\mathrm{Re} = 3000$. This corresponds to a maximum Taylor Reynolds number based on the transversal Taylor micro-scale $\mathrm{Re}_\lambda \approx 111$. The resulting turbulent flow field is, thus, expected to exhibit a clear inertial range that corresponds to the $-5/3$ Kolmogorov scaling. In the following, the setup of the DNS and the LESs of the selected Taylor–Green vortex is discussed. The DNS-solution will serve as a reference solution against which the various LES-solutions are compared.

3. Direct numerical simulation

For the DNS of the Taylor–Green vortex flow at $\mathrm{Re} = 3000$, the Equations (1) and (2) are solved on a computational grid of 384^3 nodes yielding a maximum wave number $\kappa_{max} = 192$. The equations are solved in Fourier space by a *pseudo-spectral* method [25] with anisotropic 2/3-de-aliasing for the nonlinear convective terms. Further, a pressure-correction algorithm is applied in combination with an explicit low-storage six-stage low-dissipation Runge–Kutta method [32]. A time-step $\Delta t = 0.005$ was applied, such that the corresponding *Courant-Friedrichs-Lewy* number does not exceed 0.3. The flow is simulated up to $t = 20$, requiring 4000 time steps.

Figure 1 gives an illustration of the vortex evolution of the flow, using the λ_2 criterion of Jeong and Hussain [33]. It is clear from these images that well-organized large-scale flow develops into turbulence characterized by a wide range of small-scale structures. The temporal development of the energy spectrum related the resolved velocity field $u\,(x, t = t_j)$ is shown in Figure 2(a). It is seen that the energy spectrum develops from a single characteristic Fourier mode, i.e., a single large-scale vortex, toward an entire range of modes, representing a spectrum of turbulent scales. The energy spectrum obtained at the peak of the dissipation rate, i.e., at time $t = 9$, as will be shown below, is presented in Figure 2(b).

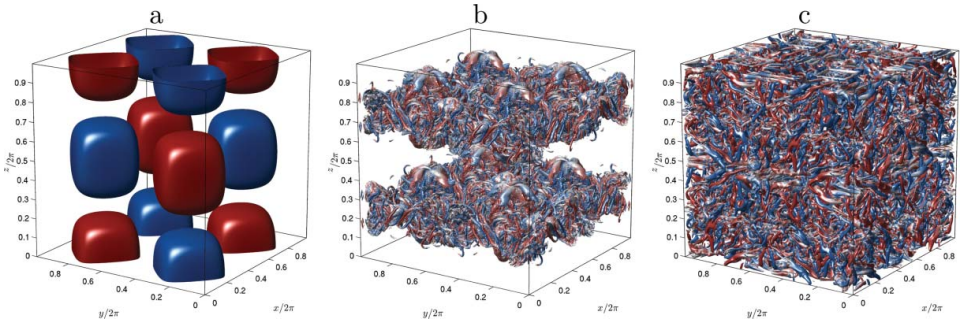

Figure 1. DNS of a Taylor–Green vortex at Re = 3000 on a 384^3 grid. Turbulent vortex structures obtained with the λ_2 criterion of Jeong and Hussain [33], and colored by z-vorticity (a) $t = 0$, (a) $t = 9$, (c) $t = 18$.

This figure also includes the results, obtained from the DNS on a computational grid of 256^3 nodes. The latter grid resolution corresponds with that of Brachet et al. [24]. The figure shows the presence of a $\kappa^{-5/3}$ inertial range in the energy spectrum. The temporal evolution of the decaying kinetic energy and the dissipation rate are shown in Figure 3. One observes that the dissipation rate $\varepsilon(t)$ rises relatively sharply around $t \geq 4$ and reaches a maximum at $t = 9$. Brachet et al. [24] reported that the Taylor–Green flow pattern becomes heavily distorted around $t = 7$, which may be interpreted as *turbulence*. The coherent structure itself, finally breaks down around $t = 8$. Therefore, it is expected that for $t \geq 9$, the flow is fully turbulent and nearly-isotropic [25].

It is verified that the evolution of the dissipation rate $\varepsilon(t)$ and the kinetic energy $k(t)$, obtained from our 384^3 DNS, are in close agreement with those obtained by Brachet et al. [24] obtained from a 256^3 DNS at the same Reynolds number. However, the kinetic energy is slightly higher and the dissipation rate is visibly lower in the 384^3 DNS. To discuss the origin of these discrepancies, the results obtained from a 256^3 DNS, carried

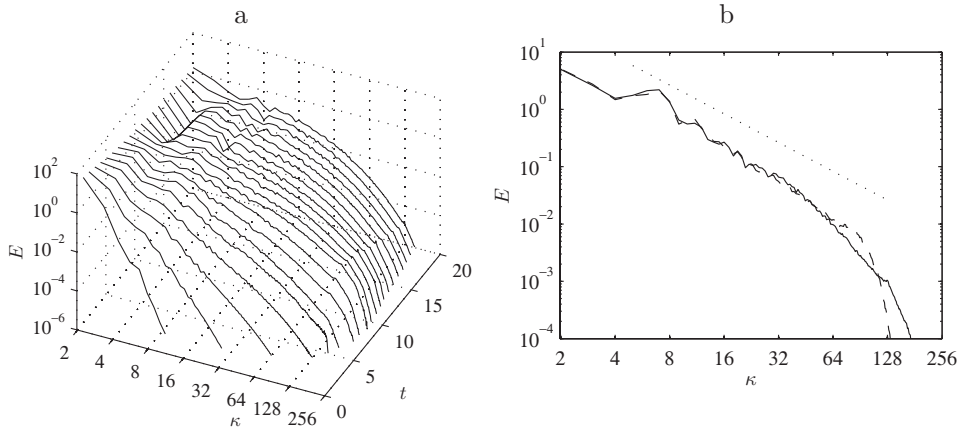

Figure 2. DNS of a Taylor–Green vortex at a Reynolds number of 3000: (a) time evolution of energy spectra obtained from the 384^3 DNS; (b) energy spectra obtained at $t = 9$ from DNS using – – – 256^3 and ——— 384^3 nodes. The dotted line represents a $\kappa^{-5/3}$ decay.

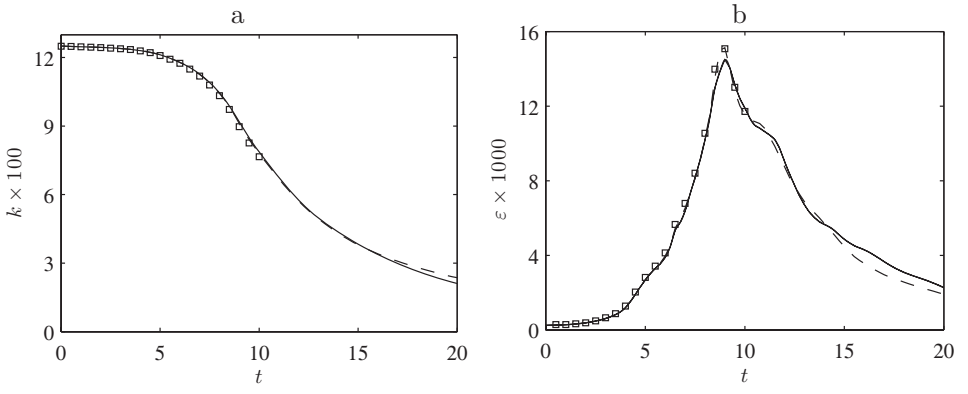

Figure 3. Time evolution of (a) the kinetic energy k and (b) the dissipation rate ε obtained from the present $- - -$ 256^3 and ——— 384^3 DNS, □ the 256^3 DNS by Brachet et al. [24].

out using our pseudo-spectral solver, are shown in Figure 3. They nearly collapse with the data of Brachet et al. [24]. This agreement demonstrates the validity of our DNS solver while suggesting that a 256^3 node resolution may not be fully sufficient for the DNS of the Taylor–Green vortex at $\mathrm{Re} = 3000$. Therefore, the 384^3 DNS results will be used as reference solutions in the following sections. In order to compare the DNS results with the LES results, for the same range of resolved scales, both the DNS data and the LES data (if necessary) will be filtered in post-processing to an identical effective resolution of 8^3, 16^3, or 64^3 computational nodes, using an anisotropic sharp Fourier filter (Fourier modes for which $\kappa_i > \kappa_{max},\ i = 1, 2, 3$ are set to zero). The filtered DNS data are shown in Figure 4.

4. Large-eddy simulation

The governing equations for the LES are obtained by applying a convolution filter to the Navier–Stokes equations (1) and (2). In the current context of the Taylor–Green flow in a homogeneous periodic box, the sharp cutoff filter $\mathscr{G}(\mathbf{x}, \kappa_c)$ is favored, with κ_c being the

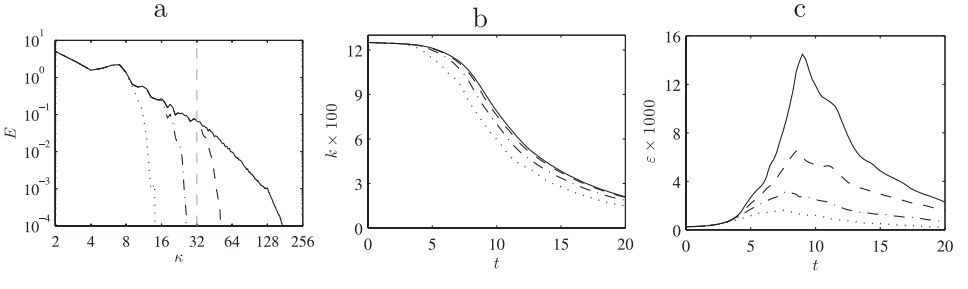

Figure 4. (a) Filtered DNS-energy spectra at $t = 9$; (b) Time evolution of the filtered DNS kinetic energy; (c) Time evolution of the filtered DNS dissipation rate. 384^3 DNS data (———); DNS data filtered at resolution 64^3 $(- - -)$; DNS data filtered at resolution 32^3 $(- \cdot - \cdot)$; DNS data filtered at resolution 16^3 $(\cdots)$.

cutoff wavenumber. The filtered Navier–Stokes equations (1) and (2) are then obtained as

$$\frac{\partial \overline{u}_i}{\partial x_i} = 0, \tag{7}$$

$$\frac{\partial \overline{u}_i}{\partial t} + \frac{\partial \overline{u}_i \overline{u}_j}{\partial x_j} + \frac{\partial \tau_{ij}}{\partial x_j} = -\frac{\partial \overline{p}}{\partial x_i} + \nu \frac{\partial^2 \overline{u}_i}{\partial x_j^2}, \tag{8}$$

where $\overline{p}(\mathbf{x}, t)$ denotes the filtered pressure field and $\tau_{ij} = \overline{u_i u_j} - \overline{u}_i \overline{u}_j$ denotes the *residual-stress* tensor. Since the smallest dissipative motions remain unresolved in LES, their statistically dissipative effect on the larger resolved scales, represented by the residual stress tensor τ_{ij} must be taken into account by means of a proper dissipative model or mechanism. If not, an energy pile-up will occur around the cutoff wavenumber κ_c, due to the spectral blockage of the computational grid, making the simulation unreliable and even unstable.

4.1. *Relaxation filtering*

In the present work, the RF approach is used to account for the residual stresses. As described in the introduction, the energy in the residual stresses is relaxed, by filtering each LES-velocity component every n^{th} time step in each Cartesian direction, using a standard finite difference filter, characterized by a specific order of accuracy m, and a fixed filtering strength σ.

The smooth three-dimensional anisotropic convolution filter kernel $\mathcal{G}(\mathbf{x}, \sigma)$, with σ the filter strength, can be written as a the convolution product of three one-dimensional filter kernels, such that

$$\mathcal{G}(\mathbf{x}, \sigma) = \mathcal{G}(x_1, \sigma) * \mathcal{G}(x_2, \sigma) * \mathcal{G}(x_3, \sigma). \tag{9}$$

The one-dimensional filtering operation of a generic variable φ in Cartesian direction $i = 1, 2, 3$ is then defined as

$$\widetilde{\varphi}(x_i) = \varphi(x_i) - \sigma \sum_{j=-n}^{n} d_j \varphi(x_{i,j}), \quad \sigma \in [0, 1], \tag{10}$$

where $\widetilde{\varphi}$ denotes the filtered variable, and $d_j = -d_{-j}$ represents the weighting coefficients that determine the dissipative contribution of the $(2n + 1)$-point symmetric finite difference filter. Note that the stencil width $(2n + 1)$ determines the order of the filter m. It is obvious that for $\sigma = 0$, the filter operator reduces to the identity operator, whereas for $\sigma = 1$, the full filter strength is engaged. Assume that RF is applied to the velocity field components each τ time levels, in order to eliminate or model the residual-stress tensor, and obtain the desired LES solution $\overline{u}_i$. Hence, the corresponding 2-step algorithm at time level T can be written as

$$\overline{u}_i^* = \overline{u}_i^T - \Delta t \left\{ \frac{\partial \overline{u}_i^T \overline{u}_j^T}{\partial x_j} + \frac{\partial \overline{p}^T}{\partial x_i} - \nu \frac{\partial^2 \overline{u}_i^T}{\partial x_j^2} \right\}, \tag{11}$$

$$\overline{u}_i^{T+1} = \mathcal{G}(\mathbf{x}, \sigma, \chi_d) * \overline{u}_i^*, \tag{12}$$

in which the *discrete* relaxation frequency function $\chi_d(T,\theta)$ is unity at time levels where the RF must be applied, and remains zero at other times. This algorithm may be interpreted as a predictor–corrector method. Indeed, in the first step a prediction of the velocity field $\overline{u}_i^*$ at the new time level is obtained, by integrating the momentum equations without taking the residual stress force into account. Because the residual stresses are neglected, $\overline{u}_i^*$ displays a slight energy pile-up near the cutoff wavenumber. This is remedied in the subsequent correction step. The predicted velocity field $\overline{u}_i^*$ is corrected by applying the relaxation filter $\mathscr{G}(\mathbf{x},\sigma,\chi)$, resulting in the velocity field $\overline{u}_i^{T+1}$ at time level $T+1$. In order to illustrate the relation with traditional LES models, we decompose the smooth filter kernel as

$$\mathscr{G}(\mathbf{x},\sigma) = \mathscr{I} - \chi_d(T,\theta)\,\mathscr{D}(\mathbf{x},\sigma), \tag{13}$$

in which $\mathscr{I}$ and $\mathscr{D}(\mathbf{x},\sigma)$ denote the identity operator and the dissipative kernel of the three-dimensional filter kernel $\mathscr{G}(\mathbf{x},\sigma)$, respectively. The discrete function $\chi_d(T,\theta)$ can be formulated mathematically as a discrete Dirac-Comb, yielding

$$\chi_d(T,\theta) = \sum_k \delta(T-k\theta) = \begin{cases} 1 & T = k\theta,\ \forall k \in \mathbb{N} \\ 0 & T \neq k\theta,\ \forall k \in \mathbb{N} \end{cases}. \tag{14}$$

It is easily understood that at time levels $T = k\theta, k \in \mathbb{N}$, the dissipative kernel $\mathscr{D}(\mathbf{x},\sigma)$ is engaged and RF is, thus, applied with unity magnitude, whereas for time levels $T \neq k\theta, k \in \mathbb{N}$, the relaxation filter reduces to the identity operator $\mathscr{I}$.

Using relation (13), it is possible to reconstruct the original equations for LES from the discrete predictor–corrector formulation (11)-(12), yielding

$$\frac{\partial \overline{u}_i}{\partial t} = -\frac{\partial \overline{u}_i \overline{u}_j}{\partial x_j} - \frac{\partial \overline{p}}{\partial x_i} + \nu \frac{\partial^2 \overline{u}_i}{\partial x_j^2} + \lim_{\Delta t \to 0} \frac{\chi_d(T,\theta)}{\Delta t}\mathscr{D}(\mathbf{x},\sigma) * \overline{u}_i^*. \tag{15}$$

Using the scaling property of the Dirac function, the residual stress force is transformed to time space as

$$\frac{\partial \tau_{ij}}{\partial x_j} = \lim_{\Delta t \to 0} \sum_k \frac{\delta(T-k\theta)}{\Delta t}\mathscr{D}(\mathbf{x},\sigma) * \overline{u}_i^* \tag{16}$$

$$= \lim_{\Delta t \to 0} \sum_k \delta(T\Delta t - k\theta\Delta t)\mathscr{D}(\mathbf{x},\sigma) * \overline{u}_i^* \tag{17}$$

$$= \sum_k \delta(t-k\tau)\,\mathscr{D}(\mathbf{x},\sigma) * \overline{u}_i \tag{18}$$

$$= \chi_c(t,\tau)\,\mathscr{D}(\mathbf{x},\sigma) * \overline{u}_i. \tag{19}$$

Hence, the *discrete* relaxation frequency function $\chi_d(T,\theta)$ becomes the *discontinuous* relaxation frequency function $\chi_c(t,\tau)$, in which the continuous time $t = T\Delta t$ and analogously physical time-scale $\tau = \theta\Delta t$. Note that expression (19) is independent of the time step Δt, but relies on the predefined time-scale τ that determines the models filtering frequency. Expressions (15) and (19) suggest a relation between the subgrid force due to RF, the penalization term in the ADM of Stolz et al. [1,13], and hyperviscosity models.

Indeed, although expression (19) for the residual stresses is a discontinuous time-function, implying that the dissipative operator is engaged after each time-scale τ at full

strength, it is possible to redefine the model into a continuous time-function, such that the operator is applied constantly at a reduced strength χ. This strength χ is obtained as the time-average of the relaxation frequency function $\chi_c(t,\tau)$, i.e.

$$\chi = \frac{1}{\tau}\int_{(k-1/2)\tau}^{(k+1/2)\tau} \chi_c(t,\tau)\,dt = \frac{1}{\tau}. \tag{20}$$

Using expressions (10) and (20), the residual stress force (19) is then worked out as

$$\begin{aligned}\frac{\partial \tau_{ij}^t}{\partial x_j} = \chi\,\{&\sigma\,[\mathscr{D}(x_1)+\mathscr{D}(x_2)+\mathscr{D}(x_3)]*\overline{u}_i + \sigma^2[\mathscr{D}(x_1)*\mathscr{D}(x_2)\\ &+\mathscr{D}(x_2)*\mathscr{D}(x_3)+\mathscr{D}(x_1)*\mathscr{D}(x_3)\,]*\overline{u}_i\\ &+\sigma^3\,[\mathscr{D}(x_1)*\mathscr{D}(x_2)*\mathscr{D}(x_3)]*\overline{u}_i\,\}.\end{aligned} \tag{21}$$

The relaxation frequency χ can, thus, be interpreted as applying the filter with kernel $[\mathscr{I}-\mathscr{D}(\mathbf{x},\sigma)]$ every $1/\chi\Delta t$ time steps. Such a formulation is entirely equivalent to the penalty term of Stolz et al. [1,13], which is a well accepted residual-stress model. It was shown by these authors, that the sensitivity of the numerical results to the precise value of the relaxation frequency χ, and thus τ, is rather weak. We emphasize that the relaxation time-scale τ is a pre-defined physical model-parameter, which is not directly related to the choice of the time step. However, it is obvious that for a chosen value of τ, decreasing the time step Δt in the algorithmic expressions (11) and (12) must be compensated by a proportional increase of θ, and vice versa. Since $\theta \geq 1$, τ is bounded as $\tau \geq \Delta t$.

It is also possible to reformulate the relaxation frequency χ as a combination of the grid spacing Δ and a constant artificial or turbulent viscosity ν_t, such that

$$\nu_t = \Delta^2\chi. \tag{22}$$

Substitution of this into the expression (21) for the residual stress force, yields

$$\begin{aligned}\frac{\partial \tau_{ij}^t}{\partial x_j} = \nu_t\Bigg\{&\sigma\,\frac{[\mathscr{D}(x_1)+\mathscr{D}(x_2)+\mathscr{D}(x_3)]}{\Delta^2}*\overline{u}_i\\ &+\sigma^2\frac{[\mathscr{D}(x_1)*\mathscr{D}(x_2)+\mathscr{D}(x_2)*\mathscr{D}(x_3)+\mathscr{D}(x_1)*\mathscr{D}(x_3)]}{\Delta^2}*\overline{u}_i\\ &+\sigma^3\frac{[\mathscr{D}(x_1)*\mathscr{D}(x_2)*\mathscr{D}(x_3)]}{\Delta^2}*\overline{u}_i\Bigg\},\end{aligned} \tag{23}$$

which is readily recognized as a eddy-viscosity-type model. However, the spatial filtering operators acting on the intermediate velocity field $\overline{u}_i^*$ are obviously more complex than the typical Laplacian operator found in traditional eddy-viscosity models. Indeed, formal Taylor-series expansion of the dissipative operators $\mathscr{D}(x_i)$, $i=1,2,3$ in the first term of expression (23), yields

$$\frac{\mathscr{D}(x_1)+\mathscr{D}(x_2)+\mathscr{D}(x_3)}{\Delta^2}*\overline{u}_i = \sum_k \beta_k \Delta^{2k-2}\frac{\partial^{2k}\overline{u}_i}{\partial x_j^{2k}}, \tag{24}$$

in which β_k denotes the Taylor-series-coefficients. Expansion (24) clearly contains a sum of high-order Laplacians, similarly to hyperviscosity models. However, in addition to these high-order Laplacians, multiple terms, involving σ^2 and σ^3, arise, which contain mixed derivatives. This is clearly different than for traditional hyperviscosity models. However, dissipative operators as (23) are often used as an *Artificial Selective Damping* in numerical simulations of aeroacoustics problems [34,35]. We note that for the lowest filter-order used in this work, $m = 4$, the dominant terms in series expansion (24) scale as Δ^2. This implies that for an infinitely fine grid with $\Delta \to 0$, the dissipation due to RF vanishes. In case of DNS resolution, the partial derivatives in Equation (24) become very small, making the residual stress dissipation negligible in comparison with the molecular dissipation.

Further, it is clear from expressions (21) and (23) that the filtering strength σ influences the magnitude of dissipative operator. However, in contrast to, e.g., the filtering frequency χ, it influences the magnitude of the different dissipative operators in expressions (21) and (23), in a nonlinear way.

Although the described predictor–corrector strategy (11)–(12) is closely related to the ADM, and hyperviscosity models, it has two advantages over these classic approaches. The major advantage of the described method is its simplicity and computational efficiency. Indeed, the two-step algorithm, and in particular the filtering action at each τ time steps, is a much easier and more efficient implementation than, e.g., the evaluation of the ADM-penalty term each Runge–Kutta sub-step, especially if the Van Cittert procedure would be used to construct a dissipative operator through iterative deconvolution. Second, the current implementation implicitly allows to model flow anisotropy, since in theory, the strength of each filter kernel $\mathcal{G}(x_1, \sigma)$, $\mathcal{G}(x_2, \sigma)$, or $\mathcal{G}(x_3, \sigma)$ can be chosen independently of each other. Although this is not the subject of this study, it is an advantage over more classic methods which often implicitly assume isotropy.

The objective in this work is now to find an appropriate smooth relaxation filter kernel $\mathcal{G}(\mathbf{x}, \sigma)$, by varying the filter order m and the strength σ, such that the spectral distribution and the global amount of dissipation in the RF method corresponds well to that of the residual stresses. Moreover, the sensitivity of the RF to variations of σ and m is investigated. We emphasize that the focus of this work is specifically on the role of m and σ. Since the influence of the RF frequency χ on the results is found to be very similar to that of σ despite their different origin (see Appendix B), we do not explicitly discuss this parameter. Stolz et al. [1,13] stated that in order to guarantee stability, the upper bound of the relaxation frequency should be close to the inverse time-step based on the CFL criterion. Muller et al. [36] identified the transfer function and the relaxation frequency in order to recover the theoretical spectral eddy viscosity. Nevertheless, Stolz et al. [13] showed that the sensitivity of the result to the specific value of the relaxation frequency χ is rather limited for the ADM. Hence, we define *a priori* $\tau = \Delta t$, implying that $\theta = 1$ or that the relaxation filter is applied every time step. Note that χ remains invariant in the current study. Since the effect of χ appears to be similar to that of σ, we expect that the value of σ will be of minor importance.

4.2. *Parametric study*

In the present work, 36 LESs of the Taylor–Green vortex flow at $\mathrm{Re} = 3000$ ($\mathrm{Re}_\lambda \approx 111$) are performed, each using an explicit standard centered finite-difference filter with different order m and different strength σ. The RF of the velocity components is applied every time step, so $\tau = 1$ in the correction step (12). The 6×6 simulations are determined by various combination of filter orders $m = 4, 6, 8, 10, 12$, and 14 with the filtering strengths

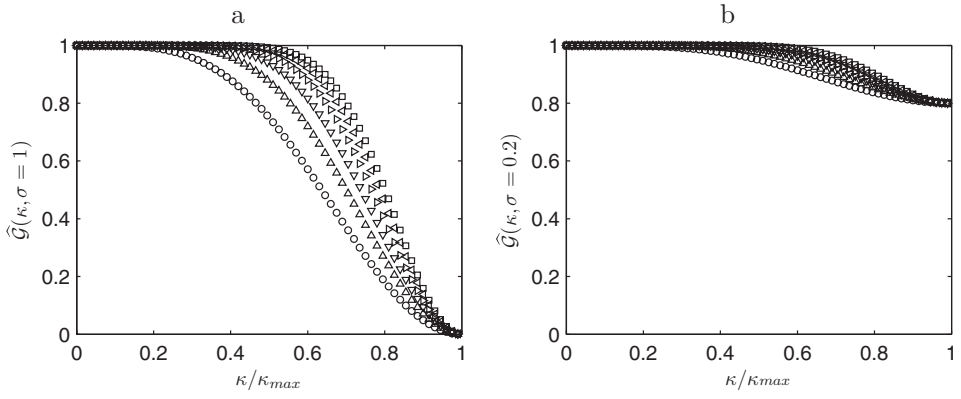

Figure 5. Transfer functions of the relaxation filters $\mathcal{G}(\mathbf{x}, \sigma)$ as a function of the wave number κ/κ_{max}: filter orders $\circ$ 4, $\triangle$ 6, $\triangledown$ 8, $\triangleright$ 10, $\triangleleft$ 12, $\square$ 14, for a filtering strength (a) $\sigma = 1$, (b) $\sigma = 0.20$.

$\sigma = 0.15, 0.2, 0.4, 0.6, 0.8,$ and 1. The weighting coefficients d_j used in relation (10), which determine the dissipative contribution of the standard symmetric finite difference filters of orders $m = 4, 6, 8, 10, 12,$ and 14, are given in Table A1 in Appendix A. The transfer functions of the various relaxation filters, for $\sigma = 0.20$ and 1 are displayed in Figure 5. It can be understood from these plots that altering the magnitude of the filtering strength σ, both influences the smoothness of the filters and the effective filter cutoff. Indeed, the filter smoothness, determined by $\frac{\partial \widehat{\mathcal{G}}(\kappa,\sigma)}{\partial \kappa}$ decreases in the entire wavenumber range when σ decreases. On the other hand, the effective filter cutoff, i.e., the wavenumber above which $\widehat{\mathcal{G}}(\kappa, \sigma)$ departs a predefined fraction from unity, increases when decreasing the strength σ. Each LES is performed on a uniform computational grid with 64^3 nodes and with grid cutoff wavenumber $\kappa_{max} = \pi/\Delta = 32$. The LES-Equations (7) and (8) are solved with the same pseudo-spectral solver, used for the DNS. We note that in this work, the relaxation filter is assumed to take dealiasing into account. Hence, no explicit dealiasing filter was applied for the LESs. The time stepping is performed again with the explicit low-dissipation 6-stage Runge–Kutta method using a time step $\Delta t = 0.025$, such that $\mathrm{CFL}_{max} = 0.25$. The relaxation filters are implemented in Fourier space, making use of their known transfer functions. In order to illustrate the *absolute* performance of the RF methods in comparison with more traditional methods, results obtained with a dynamic Smagorinsky model are also included in the plots. We used a sharp Fourier filter with cutoff $\kappa_c = 0.5\,\kappa_{max}$ as *test-filter* for the dynamic procedure, and the skew-symmetric form of the convective terms was used. We emphasize that the dynamic procedure is most appropriate when dealing with a transitional flow such as Taylor–Green, as the constant is adapted according to the spectral content of the solution.

4.3. *Post-processing*

Before assessing the performance of the RF method for LES of the Taylor–Green vortex flow, an appropriate and consistent evaluation method must be defined that allows to quantify the modeling errors. The modeling error can be obtained by comparing the DNS results with the LES results, both filtered at identical resolutions. In this perspective, the filtered DNS plays the role of an ideal LES, obtained with a perfect residual stress model. This method was first introduced by Vreman et al. [37].

To characterize the turbulence features in the LES and DNS during the flow transition from the initial Taylor–Green vortex to isotropic small-scale structures, the instantaneous isotropic energy spectra $E(\kappa, t)$ are analyzed and compared to each other, as well as the time evolutions of the resolved kinetic energy $k_r(t)$, the resolved viscous dissipation rate $\varepsilon_r(t)$, and the total dissipation rate $\varepsilon_{tot}(t)$. The resolved kinetic energy for both DNS and LES is calculated from the three-dimensional energy spectrum as

$$k_r(t) = \frac{1}{8\pi^3} \iiint_0^{\kappa_c} E(\boldsymbol{\kappa}, t)\, d\boldsymbol{\kappa}, \tag{25}$$

whereas the resolved dissipation rate is evaluated as

$$\varepsilon_r(t) = \frac{1}{8\pi^3} \iiint_0^{\kappa_c} 2\nu\boldsymbol{\kappa}^2 E(\boldsymbol{\kappa}, t)\, d\boldsymbol{\kappa}. \tag{26}$$

The subgrid dissipation rate and the total dissipation rate in LES are obtained using following relations for turbulent flows in a periodic box

$$-\frac{dk_r}{dt}(t) = \varepsilon_r(t) + \varepsilon_{sgs}(t) = \varepsilon_{tot}(t). \tag{27}$$

In order to study the accuracy of the RF method for different scale ranges in the solution, the cutoff wavenumber κ_c in expressions (25) and (26) is set to $\kappa_c = \kappa_{max} = 32$, $\kappa_c = \kappa_{max}/2 = 16$ and $\kappa_c = \kappa_{max}/4 = 8$, corresponding to the effective grid resolutions 16^3, 32^3, and 64^3, respectively. In this way it is possible to isolate the performance of the RF for large-scale statistics, and small-scale statistics of the flow. For instance, for $\kappa_c = 8$, we only focus on the accuracy of the largest resolved scales at $\kappa \leq 8$, whereas for $\kappa_c = 16$ the focus is on large and medium scales at wavenumbers $\kappa \leq 16$. For $\kappa_c = 32$, the focus is on the accuracy of all resolved scales in the LES.

To quantify the LES accuracy, and its sensitivity to the RF parameters, error landscapes are computed as function of the filtering order m and strength σ. We define the following error norms on the Longitudinal Integral Length scale $\Delta L_{11}(t)$, the resolved kinetic energy $\Delta k_r(t)$, and the resolved dissipation rate $\Delta\varepsilon_r(t)$.

$$\Delta L_{11}(t) = \frac{3\pi}{4} \left| \iiint_0^{\kappa_c} \boldsymbol{\kappa}^{-1} \left[\frac{E_{dns}(\boldsymbol{\kappa}, t)}{k_{dns}(t)} - \frac{E_{les}(\boldsymbol{\kappa}, t)}{k_{les}(t)} \right] d\boldsymbol{\kappa} \right|, \tag{28}$$

$$\Delta k(t) = \frac{1}{8\pi^3} \left| \iiint_0^{\kappa_c} [E_{dns}(\boldsymbol{\kappa}, t) - E_{les}(\boldsymbol{\kappa}, t)]\, d\boldsymbol{\kappa} \right|, \tag{29}$$

$$\Delta\varepsilon(t) = \frac{1}{8\pi^3} \left| \iiint_0^{\kappa_c} 2\nu\boldsymbol{\kappa}^2 [E_{dns}(\boldsymbol{\kappa}, t) - E_{les}(\boldsymbol{\kappa}, t)]\, d\boldsymbol{\kappa} \right|. \tag{30}$$

Just like before, the cutoff wavenumber κ_c in these expressions is set to $\kappa_c = 8$, $\kappa_c = 16$, and $\kappa_c = 32$, corresponding to the effective grid resolutions 16^3, 32^3, and 64^3.

5. Results and discussion

5.1. *A priori assessment of relaxation filtering*

The quality of the LES is first investigated via a one-dimensional a priori analysis, in which the transfer functions of the viscous contribution in the Navier–Stokes equations with that of the residual stress force that corresponds with the relaxation filtering, are compared in Fourier space. This approach, proposed by Bogey et al. [20] enables to determine a demarcation scale at which the residual stress force becomes influential and allows to study the spectral distribution of the residual stress dissipation in comparison with the molecular dissipation. Such an analysis is equivalent with evaluating the ratio of the spectral turbulent viscosity to the molecular viscosity, which is common practice in case of traditional eddy-viscosity type models. For the sake of completeness, we also compare the transfer functions of the residual stress force with the transfer function related to the spectral eddy-viscosity model of Chollet and Lesieur [38]. The one-dimensional equivalent of the transfer function of the viscous contribution is given by expression

$$G_\nu = \nu\kappa^2 = \nu\frac{\pi^2\kappa^2}{\kappa_{max}^2}\frac{1}{\Delta^2}, \tag{31}$$

whereas the one-dimensional transfer function of the spectral eddy-viscosity yields

$$G_{\nu,e} = \nu_e\kappa^2 = C_k^{-\frac{3}{2}}\left[0.441 + 15.2e^{-3.03\frac{\kappa_c}{\kappa}}\right]\sqrt{\frac{E(\kappa_c,t)}{\kappa_c}}\frac{\pi^2\kappa^2}{\kappa_{max}^2}\frac{1}{\Delta^2}, \quad C_k = 1.5. \tag{32}$$

Here, the cutoff wavenumber is chosen as $\kappa_c = 32$, in conformity with the LES simulations in this work, whereas the energy content of the cutoff Fourier mode $E(\kappa_c, t)$ is obtained from the DNS data at $t = 9$. The one-dimensional equivalent of the transfer function of the residual stress force (19) can be written as

$$G_{rf} = \frac{\sigma}{\tau}\widehat{\mathscr{D}}\left(\frac{\pi^2\kappa^2}{\kappa_{max}^2}\right), \tag{33}$$

with $\widehat{\mathscr{D}}(\kappa)$ the dissipative part of the relaxation filter in Fourier space. Note that there is no dispersive part of the filter due to its symmetric kernel. The one-dimensional transfer functions G_ν, $G_{\nu,e}$, and G_{rf} are presented in Figure 6 for the relaxation filters of order $4 \rightarrow 14$ and strengths $\sigma = 0.2$ and $\sigma = 1$. Except for the fourth-order filter, the dissipation due to the relaxation filtering remains smaller than the molecular dissipation in the low-wavenumber region, i.e., for the largest scales in the flow. Moreover, the largest dissipation is only applied to the small scales in the high-wavenumber region, as expected. However, in comparison with the transfer function of the spectral eddy viscosity, which has a similar scaling as the molecular viscosity, the relaxation filtering induces too much dissipation on the small scales, and too little on the large scales. Similar conclusions can be drawn analyzing the nonlinear energy transfer $T(\kappa, t)$, which arises in the spectral energy balance in LES due to unresolved triadic interactions. With $E(\kappa, t)$ denoting the LES energy spectrum, the spectral energy balance is written as

$$\frac{\partial E(\kappa,t)}{\partial t} = -2\nu\kappa^2 E(\kappa,t) + T(\kappa,t), \tag{34}$$

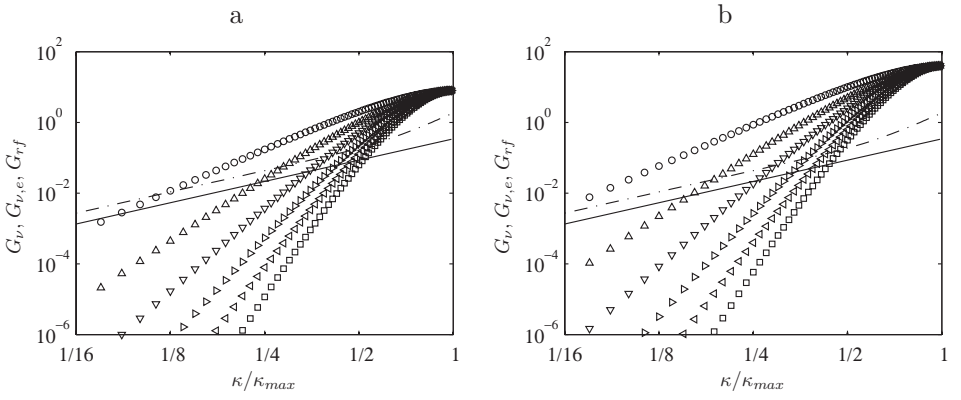

Figure 6. Transfer functions of the dissipation mechanisms in the LES as a function of the wavenumber κ/κ_{max}: ——— molecular viscosity, $-\cdot-\cdot$ spectral eddy viscosity, and relaxation filtering of order ○ 4, △ 6, ▽ 8, ▷ 10, ◁ 12, □ 14, for a filtering strength (a) $\sigma = 0.2$ and (b) $\sigma = 1$.

in which $T(\kappa, t)$ is defined as

$$T(\kappa, t) = \Re\left(-i\kappa_l \widehat{\tau}_{kl} \widehat{u}_k^*\right), \tag{35}$$

and $\widehat{u}$ and $\widehat{\tau}$ denote, respectively, the Fourier-transformed velocity field and residual stress tensor. Based on the a priori available DNS data of the Taylor–Green vortex, the exact nonlinear energy transfer $T(\kappa, t)$ due to the unresolved triadic interactions can be reconstructed. Assuming expression (19) for $T(\kappa, t)$, the energy drain for the relaxation filtering model is reconstructed using the DNS data, and also a similar evaluation can be done when assuming the constant Smagorinsky model. In addition, the spectral cross-correlation coefficient $\rho_i(\kappa, t)$, based on the correlation between the true residual stress force f_i with standard deviation σ_{f_i} and the modeled stress force f_i' with standard deviation $\sigma_{f_i'}$ and defined as

$$\rho_i(\kappa, t) = \frac{\widehat{f}_i^*(\kappa)\,\widehat{f}'_i(\kappa)}{\sigma_{f_i}\sigma_{f_i'}}, \quad i = 1, 2, 3 \tag{36}$$

is calculated. As shown in Figure 7, the relaxation filtering subgrid force displays a similar tendency as in Figure 6 when compared with the molecular dissipation, i.e., negligible dissipation for the largest scales in contrast to significant dissipation on the smallest scales. However, since the exact nonlinear energy transfer $T(\kappa, t)$ resembles the profile of the molecular dissipation, one concludes that the relaxation filtering provides too much dissipation on the small scales and too little on the large scales. On the other hand, the constant Smagorinsky model displays a similar spectral distribution as the true subgrid stress, although the standard Smagorinsky constant $C_s = 0.17$ obviously results in an overestimation of the global dissipation. Although the subgrid force of the relaxation filtering method is less correlated with the true subgrid force than the Smagorinsky at lower wavenumbers, it is better correlated than the Smagorinsky force for the higher wavenumbers, according to this a priori analysis. Integrating $\rho(\kappa, t)$ over the wavenumber space leads to a global cross-correlation coefficient of 0.0735 for the Smagorinsky model and coefficients within the range [0.23, 0.34] for the different relaxation filters. Hence, the latter method is globally

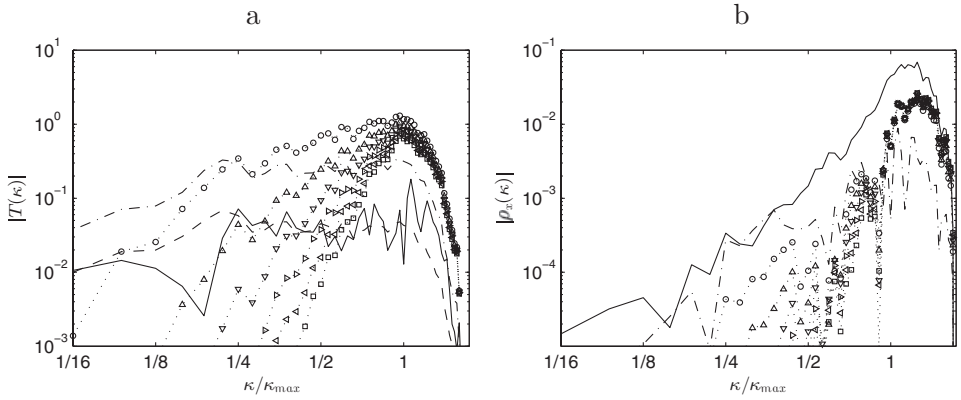

Figure 7. Nonlinear energy transfer $T(\kappa, t = 9)$ as a function of the wave number κ/κ_{max} (a) and spectral cross-correlation coefficient $\rho_x(\kappa, t = 9)$: ——— exact reconstruction, $-\cdot-\cdot$ Smagorinsky model ($C_s = 0.17$), $---$ molecular viscosity, and relaxation filtering with strength $\sigma = 0.2$ and order $\circ$ 4, $\triangle$ 6, $\triangledown$ 8, $\triangleright$ 10, $\triangleleft$ 12, $\square$ 14, for a filtering strength, (b) $\sigma = 1$.

better correlated with the true residual stress force. Since the relaxation filtering is closely related to the approximate deconvolution method and hyperviscosity models, those methods most likely display very similar behavior. Although these *a priori* results are somewhat disappointing, a much better behavior is observed when evaluating the models *a posteriori*, as will be shown further in the text. Such discrepancy between *a priori* and *a posteriori* analysis, is not uncommon in the field of turbulence modeling. Indeed it is well known that a good *a priori* correlation does not imply proper *a posteriori* results and vice versa.

Based on Figures 6(a) and 7, one notices that the critical wavenumber above which the subgrid dissipation exceeds the molecular dissipation depends on the precise choices of the filter order m and filtering strength σ. The figures seems to indicate that the filter order m is more important than the value of σ. In order to analyze the latter observation in more detail, we determine an effective cutoff wavenumber ratio κ_e/κ_{max} at the intersection of the molecular and subgrid dissipation, as a function of σ and m. As mentioned earlier, this cutoff wavenumber indicates a demarcation scale at which the residual stress model becomes influential. This is depicted in Figure 8(a). In the same way, the effective cut-off wavelength normalized by the grid size $PPW_e = \lambda_e/\Delta$ is shown in Figure 8(b). These graphs indicate that the dependency of the dissipation on the filtering strength σ is relatively small, especially once $\sigma \geq 0.4$. In contrast, the dependency on the filter order m is much larger, although the effect decreases with increasing filter order. Finally, these figures suggest that in order to limit the dissipation to the small scales in the upper half of the wavenumber range, one has to select a filter of order $m \geq 8$. The effective cut-off wavelengths are indeed around $PPW_e = 32$ for order $m = 4$, and $PPW_e = 10$ for order $m = 6$, but they are smaller than $PPW_e = 8$ for higher orders.

5.2. *A posteriori assessment of relaxation filtering*

5.2.1. *Energy spectra*

Figure 9 shows the energy spectra $E(\kappa, t = 9)$ at the peak of the dissipation rate, for all LESs and the DNS. In Figure 9(a), the energy spectra of the LES obtained with the fourth-order relaxation filter are seen to vary strongly with the filtering strength σ, and

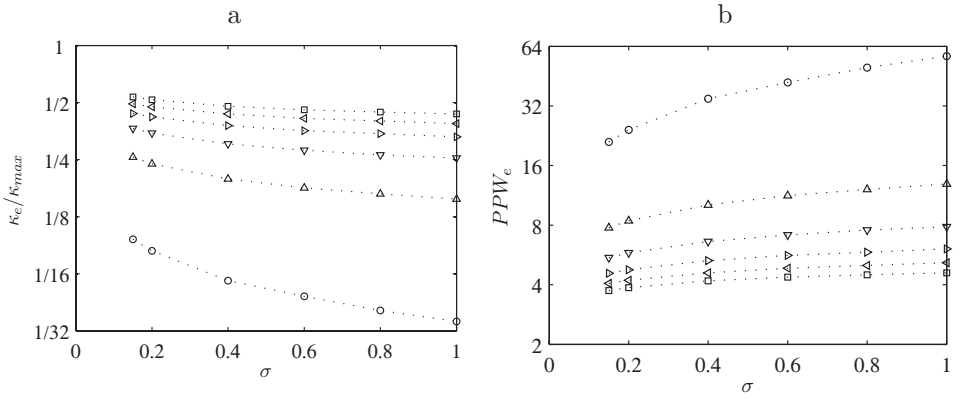

Figure 8. Variations with the filtering strength σ using RF of order $\circ$ 4, $\triangle$ 6, $\triangledown$ 8, $\triangleright$ 10, $\triangleleft$ 12, $\square$ 14 of the (a) the cut-off wavenumber κ_e/κ_{max} and (b) the cut-off wavelength $PPW_e = \lambda_e/\Delta$.

differ significantly from the DNS spectrum. More precisely, the energy of the small scales, at wavenumbers $\kappa_{\max}/8 \leq \kappa \leq \kappa_{\max}$ is obviously underestimated, whereas the energy of the large scales at wavenumbers $\kappa \leq \kappa_{\max}/8$ and thus discretized by more than 16 points per wavelength, seems overestimated. Hence, the fourth-order filtering not only appears to damp the small turbulent scales excessively, but also keeps the very large scales too strong and coherent, and prevents them from breaking up into smaller scales. Because the energy transfer from the large to small scales is disturbed, just like in a bottleneck, the very large scales suffer from an energy build-up.

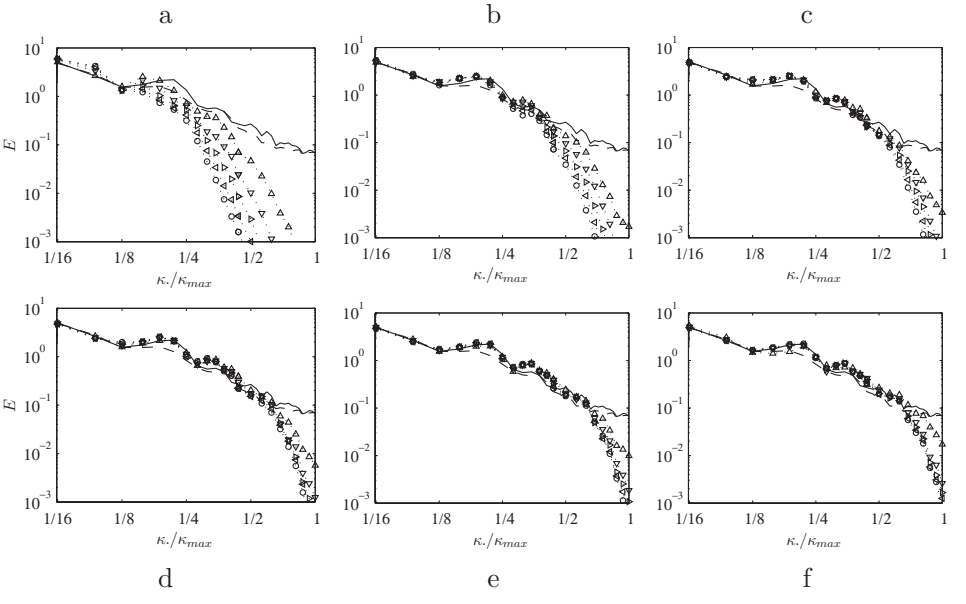

Figure 9. Energy spectra $E(\kappa, t)$ at $t = 9$ from ——— the 384^3 DNS, and from the 64^3 LES using the dynamic Smagorinsky model (− − −) and the relaxation filters of order (a) 4, (b) 6, (c) 8, (d) 10, (e) 12, and (f) 14, at strength $\triangle\ \sigma = 0.2$, $\triangledown\ \sigma = 0.4$, $\triangleright\ \sigma = 0.6$, $\triangleleft\ \sigma = 0.8$, and $\circ\ \sigma = 1$.

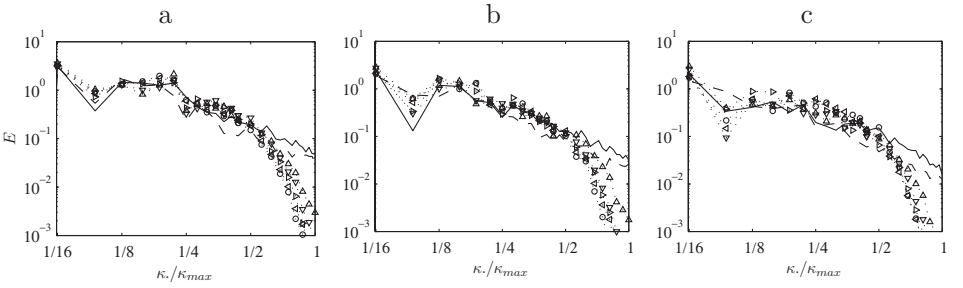

Figure 10. Energy spectra $E(\kappa, t)$ at (a) $t = 12$, (b) $t = 15$, and (c) $t = 18$ from ——— the 384^3 DNS, and from the 64^3 LES using the dynamic Smagorinsky model (− − −) and the relaxation filters of order 10 at strength $\triangle\ \sigma = 0.2$, $\triangledown\ \sigma = 0.4$, $\triangleright\ \sigma = 0.6$, $\triangleleft\ \sigma = 0.8$, and $\circ\ \sigma = 1$.

When going to higher-order relaxation filters, the dissipation on the small scales decreases, whereas the bottleneck effect vanishes. In Figure 9(c), for the filter at order $m = 8$, for instance, the LES spectra seem nearly independent of the filtering strength for $\sigma \geq 0.4$, and they correspond well to the DNS spectrum up to $\kappa \simeq \kappa_{max}/2$, that is around four points per wavelength. A similar agreement between LES and DNS spectra is noticed for the filter at order $m = 10$, 12, and 14. Note also that, when high-order filters are used with very low values of strength σ, typically $\sigma \leq 0.2$, the energy contained by wavenumbers close to κ_{max} is significant, as found for an example given in Figure 9(f). The dissipation provided by the filtering may be insufficient in this case, which might lead to an energy pile-up around the grid cutoff wavenumber, and hence to numerical instability.

Comparison of the DNS spectra with the spectra obtained with the dynamic Smagorinsky model, clearly reveals that this traditional eddy-viscosity-type model dissipates too much energy at the large and medium scales, i.e. $\kappa \leq 0.5\,\kappa_{max}$, in contrast to the relaxation filtering method with $m \geq 6$. On the other hand, the Smagorinsky model does not seem to damp the smallest resolved scales, and even a small energy pile-up may be witnessed around the grid cutoff $\kappa \approx \kappa_{max}$. This is quite different from the relaxation filtering method which significantly reduces the amplitude of those smallest resolved scales. From a mathematical point of view, scales near the grid cutoff should be damped in order to respect the Nyquist criterion. In that perspective, the use of linear modeling operators, such as the relaxation filters, might be considered advantageous.

In order to illustrate the long-time spectral behavior of the LES models, Figure 10 shows the energy spectra of the tenth-order relaxation filter at times $t = 12$, $t = 15$, and $t = 20$, that is during the stages of turbulence decay. At least for $t = 12$ and $t = 15$, the tenth-order relaxation filtering tends to outperform the dynamic Smagorinsky model for the prediction of the energy at the large and medium scales. It is witnessed that at $t = 20$, the energy of the medium scales is too high. Indeed, it is verified further in the text (Figure 15) that due to the moderate Reynolds number, the length of the inertial range decreases systematically with time due to energy decay and the absence of an external forcing. For $t > 13$, the inertial range becomes so short that the fixed LES cutoff κ_c is located at the beginning of the dissipation range. Because the filter coefficients are not adjusted dynamically in order to account for the "shifted" position of the cutoff wavenumber, the relaxation filter becomes too dissipative for the small scales, leading to a spectral blockage at the medium scales and thus an energy pile-up.

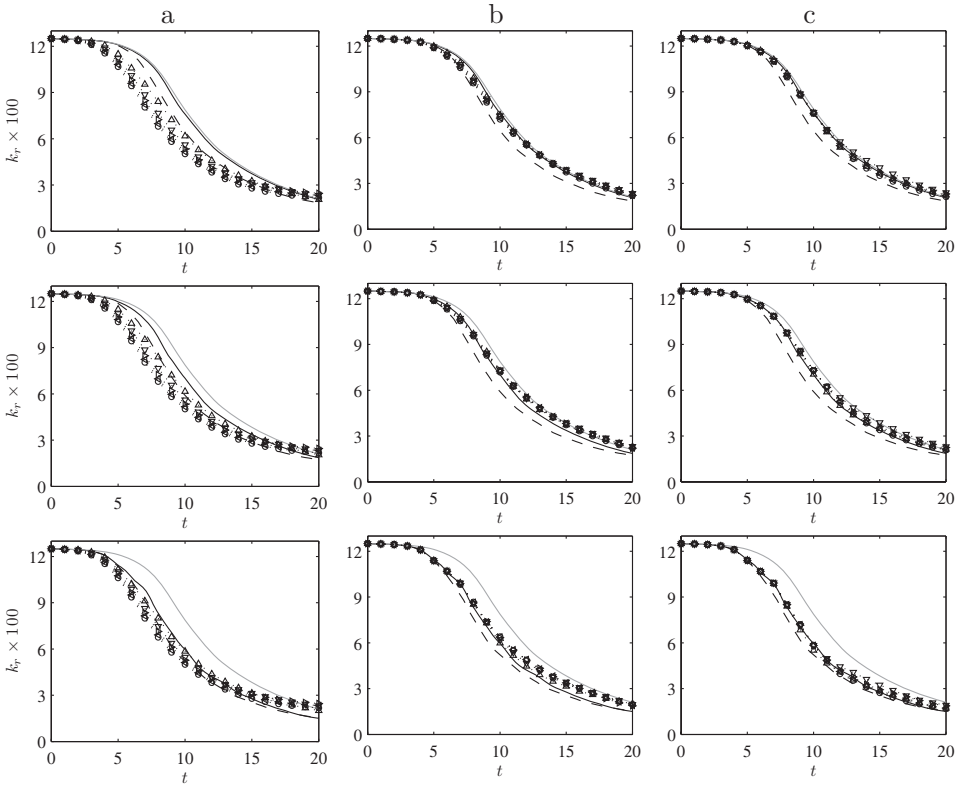

Figure 11. Time evolution of the resolved kinetic energy obtained from ——— the 384^3 DNS data, ——— the 384^3 DNS data filtered to the LES resolution, the dynamic Smagorinsky model (– – –) and the 64^3 LES using RF of order (a) 4, (b) 8, (c) 14, at strength $\triangle$ $\sigma = 0.2$, $\triangledown$ $\sigma = 0.4$, $\triangleright$ $\sigma = 0.6$, $\triangleleft$ $\sigma = 0.8$, and $\circ$ $\sigma = 1$. First row $\kappa_c = 32$, second row $\kappa_c = 16$, and third row $\kappa_c = 8$.

5.2.2. *Turbulence statistics*

The resolved kinetic energy $k_r(t)$ and the resolved dissipation rate $\varepsilon_r(t)$ for the LES cases with relaxation filters of order $m = 4$, $m = 8$ and $m = 14$ and for three different cutoff wavenumbers $\kappa_c = 32$, $\kappa_c = 16$ and $\kappa_c = 8$, are presented in Figures 11 and 12, respectively.

In Figure 11(a), as expected from the energy spectra, the excessive damping of the turbulent scales in the range $[\kappa_{max}/8, \kappa_{max}]$ due to the low-order relaxation filtering results in a too fast decay of kinetic energy in comparison with the filtered DNS reference solution. Comparison of the results for different post-processing cutoff wavenumbers, i.e. $\kappa_c = 8, 16, 32$, indicates that the energy of the very large scales ($\kappa \leq 8$) decays much slower then the energy of the medium and small scales ($\kappa > 8$). In other words, the energy drain from the smaller scales, is too large. Going to higher-order relaxation filters, the decay of kinetic energy agrees well with the filtered DNS data in Figures 11(b) and 11(c), and at larger times, it becomes even slightly overestimated. On the other hand, the Smagorinsky model severely underestimates the resolved kinetic energy in comparison with the other RF results, regardless of the value of κ_c. This indicates that the subgrid dissipation of the Smagorinsky model is too high.

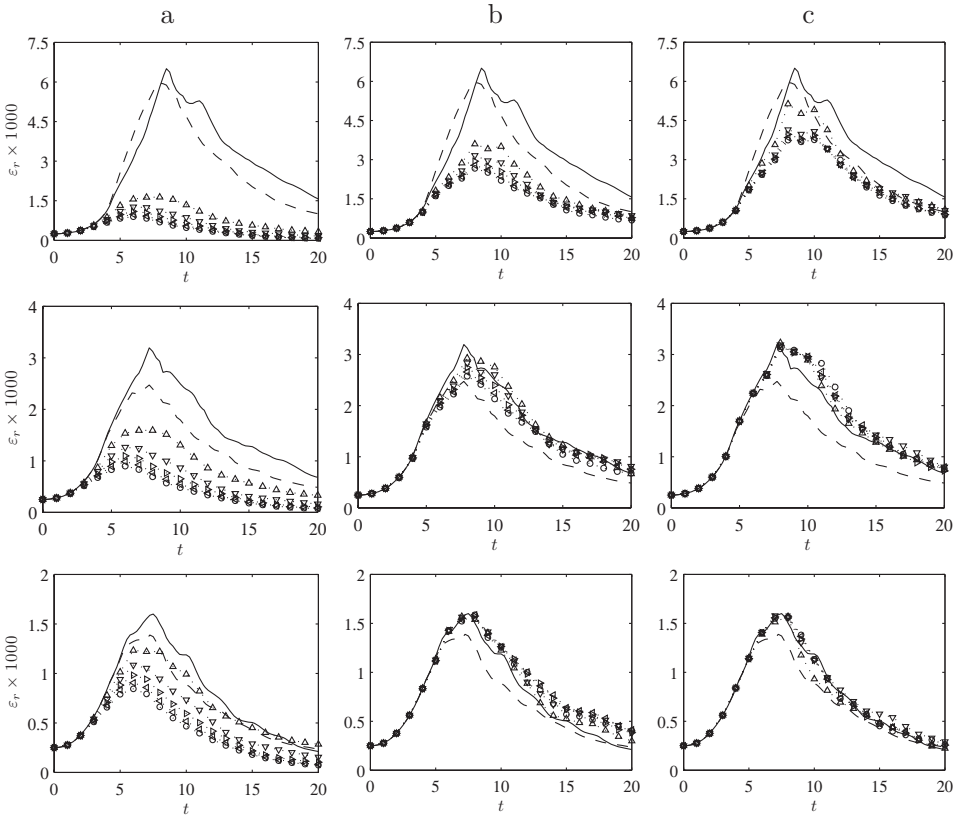

Figure 12. Time evolution of the resolved dissipation rate obtained from ——— the 384^3 DNS filtered to the LES resolution, and the 64^3 LES using the dynamic Smagorinsky model (− − −) and RF of order (a) 4, (b) 8, and (c) 14, at strength $\triangle\ \sigma = 0.2$, $\triangledown\ \sigma = 0.4$, $\triangleright\ \sigma = 0.6$, $\triangleleft\ \sigma = 0.8$, and $\circ\ \sigma = 1$. First row $\kappa_c = 32$, second row $\kappa_c = 16$, and third row $\kappa_c = 8$.

Similar observations are seen when looking at the resolved dissipation rate in Figure 12. Indeed, the use of low-order relaxation filters ($m = 4$) results in a substantial underestimation of $\varepsilon_r(t)$ in comparison with the filtered DNS results in Figure 12(a). Isolating the medium scales and large scales, by reducing κ_c to $\kappa_c = 16$ and $\kappa_c = 8$, respectively, indicates that although the resolved dissipation rate is mostly affected by errors on the medium and small scales, the large-scale errors also contribute. This implies that even the large scales at wave numbers $\kappa \leq 16$ are affected by the relaxation filtering rather than by molecular viscosity. As a consequence, their dynamics are influenced by the subgrid dissipation model, and the effective Reynolds number of the flow may be artificially lowered. In Figures 12(b) and 12(c), for the LES performed with relaxation filters of order $m = 8$ and $m = 14$, the resolved dissipation rate clearly improves, and reducing κ_c to $\kappa_c = 16$ and $\kappa_c = 8$ reveals that the error on $\varepsilon_r(t)$ is now only affected by small-scale errors. Hence, the behavior of the large and medium scales is mostly determined by molecular viscosity,which is in agreement with the *a priori* assessment of relaxation filtering presented previously. Surprisingly, the dynamic Smagorinsky model approaches the resolved dissipation rate of the total solution quite well for $\kappa_c = 32$, and even outperforms the relaxation filtering method. However, when considering only the dissipation on medium and large scales, i.e.,

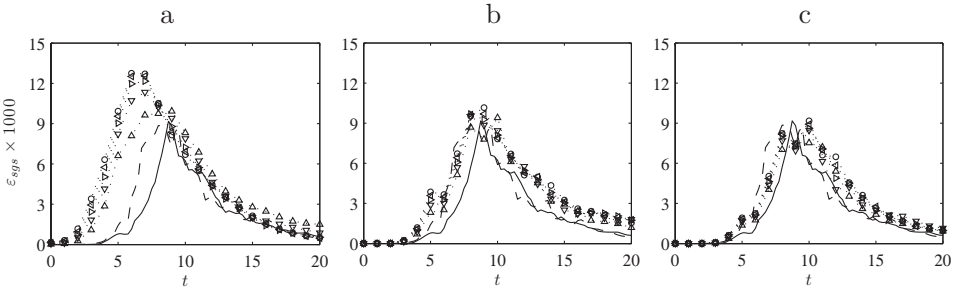

Figure 13. Time evolution of the subgrid-scale dissipation rate obtained from ——— the 384^3 DNS filtered to the LES resolution, and the 64^3 LES using the dynamic Smagorinsky model (– – –) and RF of order (a) 4, (b) 8, and (c) 14, at strength $\triangle\ \sigma = 0.2$, $\triangledown\ \sigma = 0.4$, $\triangleright\ \sigma = 0.6$, $\triangleleft\ \sigma = 0.8$, and $\circ\ \sigma = 1$.

$\kappa_c = 16$ and $\kappa_c = 8$, it becomes obvious that the Smagorinsky model dissipates too much energy, and is outperformed by the higher-order relaxation filters.

The results of $k_r(t)$ and $\varepsilon_r(t)$ thus demonstrate that in contrast to the Smagorinsky model, the relaxation filtering seems to have a limited impact on the large resolved scales, if the order m is high enough. Moreover, the dependency of the statistics on the filtering strength σ is substantial when low-order relaxation filters, such as $m = 4$, are used, but vanishes rapidly for high-order relaxation filters.

Using relation (27), it is possible to reconstruct the subgrid dissipation rate $\varepsilon_{sgs}(t)$ due to the relaxation filtering and the total dissipation rate $\varepsilon_{tot}(t)$. The evolutions of $\varepsilon_{sgs}(t)$ and $\varepsilon_{tot}(t)$ are shown in Figures 13 and 14, respectively, for the LES cases with relaxation filters of orders $m = 4, 8$, and 14, and the dynamic Smagorinsky model. The post-processing cutoff wavenumber here is $\kappa_c = \kappa_{max} = 32$, that is the LES grid cutoff wavenumber. Figures 13(a) and 14(a) clearly show that for the fourth-order relaxation filter, both the resulting subgrid dissipation and the total dissipation increase too quickly, resulting in a too fast decay of kinetic energy. This is even worse for the dynamic Smagorinsky model, where the dynamic procedure clearly engages the model too soon and too strong during the transitional stages, resulting in a severe underestimation of the kinetic energy profiles, as witnessed earlier. Using higher-order relaxation filters leads to a much better prediction of the subgrid and total dissipations. The subgrid dissipation, shown in Figures 13(b) and 13(c), is indeed close to the ideal subgrid dissipation, reconstructed from the DNS.

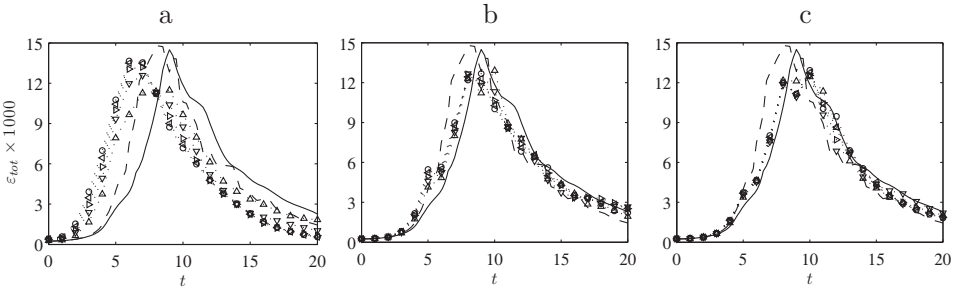

Figure 14. Time evolution of the total dissipation rate obtained from ——— the 384^3 DNS, and the 64^3 LES using the dynamic Smagorinsky model (– – –) and RF of order (a) 4, (b) 8, and (c) 14, at strength $\triangle\ \sigma = 0.2$, $\triangledown\ \sigma = 0.4$, $\triangleright\ \sigma = 0.6$, $\triangleleft\ \sigma = 0.8$, and $\circ\ \sigma = 1$.

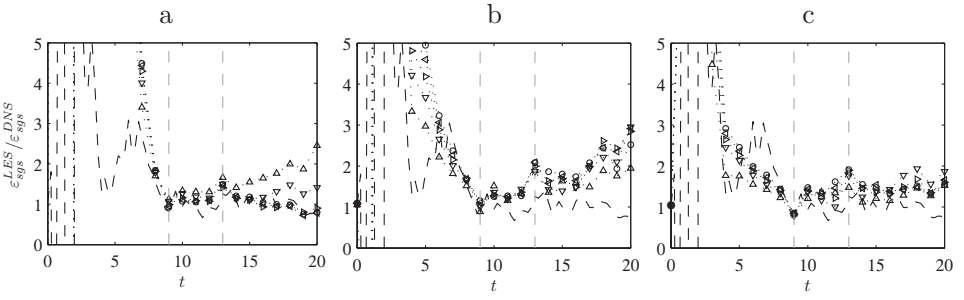

Figure 15. Time evolution of the ratio between the subgrid-scale dissipation rate obtained from the 64^3 LES and ——— the 384^3 DNS filtered to the LES resolution: dynamic Smagorinsky model (− − −) and RF of order (a) 4, (b) 8, and (c) 14, at strength △ $\sigma = 0.2$, ▽ $\sigma = 0.4$, ▷ $\sigma = 0.6$, ◁ $\sigma = 0.8$, and ○ $\sigma = 1$. The time interval in which the inertial range is sufficiently developed is indicated by the vertical dashed lines.

It also interesting to investigate the ratio between the true subgrid-scale dissipation rate from the various LES simulations and the subgrid-scale dissipation rate, reconstructed from the filtered DNS data. This is shown in Figure 15. It is verified that the mean ratio between the sgs dissipation rate obtained in the LES and the one from DNS evolves from unity at time $t = 9$, i.e., at peak dissipation rate when the inertial range is fully established, up to a value near 2 for $t = 20$. Because of the moderate Reynolds numbers, the length of the inertial range is maximal at $t = 9$, thus at peak dissipation rate, but decreases systematically with time due to energy decay and the absence of an external forcing. This implies that the inertial range is only fully developed for $t = 9 \rightarrow \pm 13$, as indicated on the figures. It is seen that the mean ratio is relatively close to unity in this interval. For $t > 13$, the predetermined LES cutoff $\kappa_c = 32$ is located at the beginning of the dissipation range. As a consequence, the relaxation filters are too dissipative resulting in a larger ratio since the final filter coefficients, responsible for the subgrid dissipation, are not adjusted by a dynamic procedure in contrast to the Smagorinsky model. As mentioned in the introduction, the objective in this work is to investigate the performance of finite difference filters with predefined coefficients, and as shown in previous figures, good agreement with the filtered DNS is obtained.

5.2.3. *Role of the filtering strength*

In the previous paragraphs, we demonstrated the role of the order m of the relaxation filter. It was observed that this factor plays a very important role in the performance of the relaxation filtering method for LES. Results also indicated that the filtering strength σ is an important parameter using low-order relaxation filters, while suggesting that it has a rather limited impact using high-order filters. In this paragraph, the variations of the LES results with the filtering strength σ and the filter order m are quantified. The resolved kinetic energy k_r and the resolved dissipation rate ε_r obtained in the LES and the DNS at time $t = 9$, i.e., when the flow is fully turbulent, are shown in Figures 16(a) and 16(b), for three different cutoff wavenumbers $\kappa_c = 32$, $\kappa_c = 16$, and $\kappa_c = 8$. The subgrid activity in the LES, defined as the ratio between the subgrid dissipation and the total dissipation

$$A_{sgs}(t) = \frac{\varepsilon_{sgs}}{\varepsilon_r + \varepsilon_{sgs}} \tag{37}$$

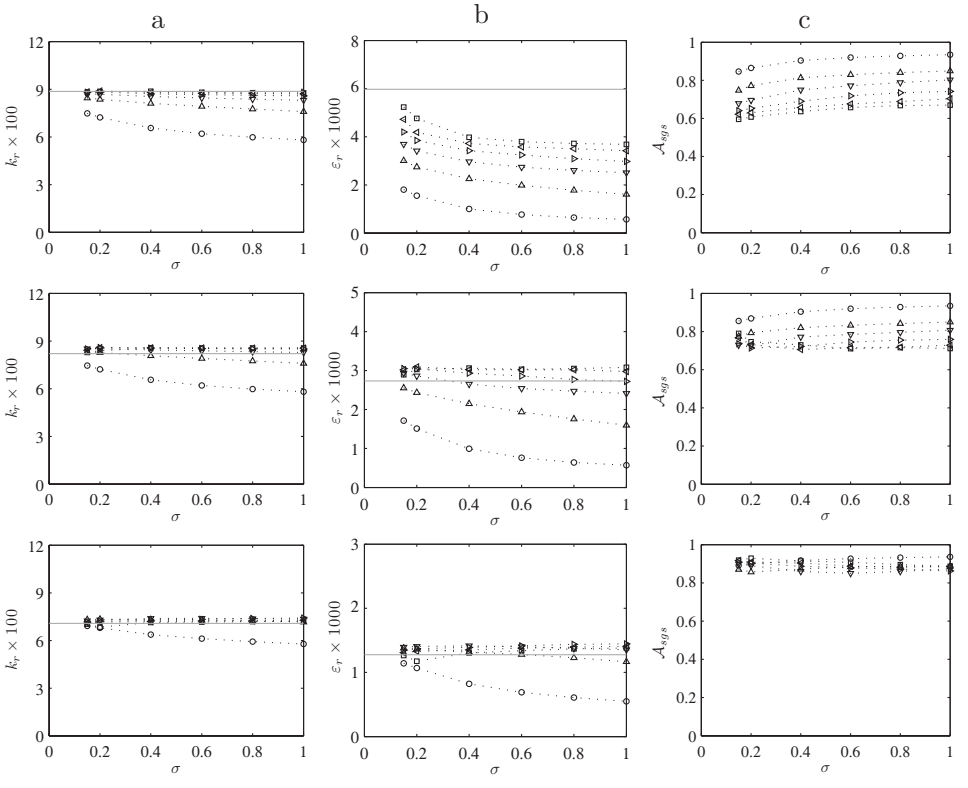

Figure 16. Variations with the filtering strength σ in the 64^3 LES using RF of order $\circ$ 4, $\triangle$ 6, $\triangledown$ 8, $\triangleright$ 10, $\triangleleft$ 12, $\square$ 14 of the: (a) resolved kinetic energy, (b) resolved dissipation, and (c) sgs activity. The gray lines indicate the values obtained in the 384^3 DNS. First row $\kappa_c = 32$, second row $\kappa_c = 16$, and third row $\kappa_c = 8$.

is also shown at time $t = 9$ in Figure 16(c). It is obvious from these figures that the filtering strength σ of the relaxation filter, which determines mainly the global dissipation magnitude, only has a minor influence on the resolved kinetic energy, the resolved dissipation rate, and the subgrid activity. Only for low values of σ, the results indicate a slight dependency of k_r, ε_r, and A_{sgs} to this parameter. However, once $\sigma \geq 0.4$, the results become nearly independent. Further, the figures demonstrate that the influence of the order m of the relaxation filter, which determines mainly the spectral distribution of the dissipation, is the dominant parameter in the method. Although the impact on the resolved kinetic energy is rather limited, it becomes significant when looking at the resolved dissipation rate and the subgrid activity. This confirms the observations from the *a priori* study. Finally, reducing the post-processing cutoff wavenumber to $\kappa_c = 16$ and $\kappa_c = 8$, shows that the influence of both parameters diminishes rapidly when looking at only the large scales in the flow. This implies that the subgrid dissipation of the relaxation filter, only influences the small scales, leaving the large scales unaffected, unless the order of the filter becomes too low, i.e., $m \leq 6$. The quality of the LES methodology is further demonstrated by the comparisons between LES and DNS results. There is a good agreement in Figure 16(a) for the resolved kinetic energy obtained at the three resolutions considered, provided that $m \geq 10$ for $\kappa_c = \kappa_{max} = 32$, that $m \geq 8$ for $\kappa_c = 16$, and that $m \geq 6$ for $\kappa_c = 8$. This is expected from the filtering cutoff

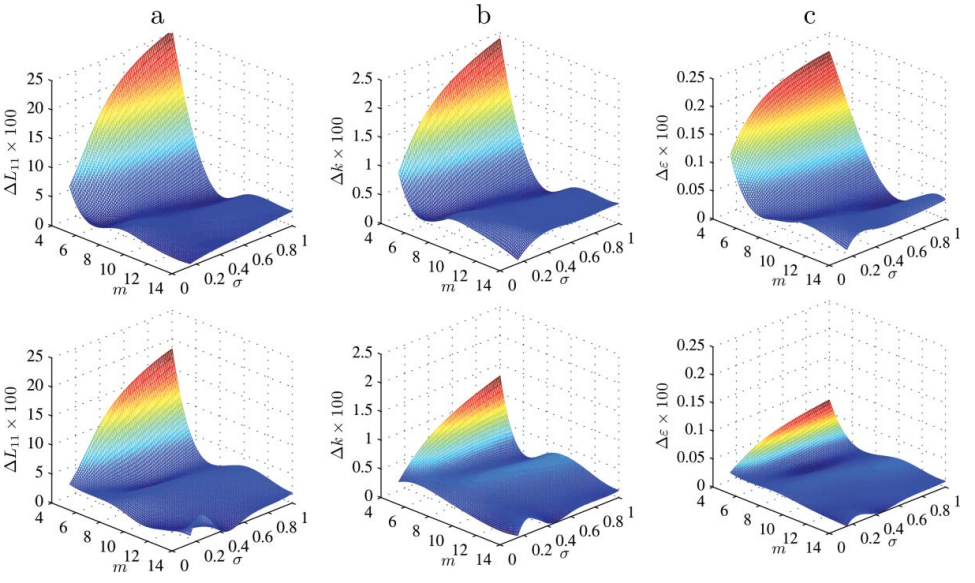

Figure 17. Error landscapes as function of filtering order m and strength σ for (a) the resolved longitudinal integral length scale, (b) kinetic energy, and (c) dissipation rate, at $t = 9$. First row $\kappa_c = 16$ and second row $\kappa_c = 8$.

wavenumbers presented in Figure 8(a). Similar agreement is observed for the resolved dissipation in Figure 16(b) for $\kappa_c = 16$ and $\kappa_c = 8$. For $\kappa_c = 32$, the resolved dissipation is lower in the LES than in the DNS, which is natural because in the LES the wavenumbers close to κ_{max} are dissipated by the relaxation filtering, and hence cannot contribute to the resolved dissipation as is the case in the DNS.

5.2.4. *Error landscapes*

Figure 17 shows the error landscapes for ΔL_{11}, Δk, and $\Delta \varepsilon$ computed between LES and DNS results at time $t = 9$, i.e., at maximum dissipation rate, as functions of the order m and strength σ of the relaxation filter for two different cutoff wavenumbers $\kappa_c = 16$ and $\kappa_c = 8$ corresponding to four and eight points per wavelength in the LES, respectively. The error landscapes support the former conclusions. Indeed, the use of low-order filters leads to significant errors that depend severely on the filtering strength σ. Applying a relaxation filter of order $m = 4$, results in large errors, even for very small values of the filtering strength, e.g., $\sigma = 0.15$. Increasing the order of the relaxation filter to $m = 6$, reduces the errors substantially, but they are still significant if $\sigma \geq 0.6$. Once the filter order $m \geq 8$, the LES results display good accuracy, regardless of the value of the filtering strength σ. Hence, we conclude once again that the precise value of the filtering strength σ is not crucial if the order m of the relaxation filter is large enough, say $m \geq 8$. Note that the error landscapes exhibit optimal error-valleys, located at $8 \leq k \leq 10$. Although the errors are nearly independent of the filtering strength σ, they depend strongly on the filtering order. Hence, the use of eighth- or 10th-order filters seems optimal for the selected test case. The use of even higher-order filters, i.e., $m \geq 10$ slightly deteriorates the results, leading to a reduction of the accuracy. Since such high-order filters ($m \geq 10$) are only effective near the

grid-cutoff wave number, the reduced accuracy stems likely from the increased contribution of aliasing errors.

6. Conclusion

In this work, a quantitative assessment of the LES method based on relaxation filtering, using standard finite difference filters with order m and adjustable strength σ, has been conducted. The Taylor–Green vortex at $\mathrm{Re} = 3000$ is selected as a representative test case. Based on the spectral *a priori* analysis, it was seen that the chosen class of relaxation filters, induce a negligible amount of dissipation on the largest resolved scales in contrast to a significant amount of dissipation on the smallest resolved scales. The spectral dissipation–distribution does not correlate well with the reconstructed subgrid force at the largest scales, although for the smallest scales, the correlation was good. Moreover, the *a priori* analysis indicated that the filter order m is more influential than the filtering strength σ. Indeed, *a posteriori* comparison with filtered DNS data, using so-called error landscapes, shows that the accuracy of the LES results depends essentially on the choice of a sufficiently sharp filter, such that the dissipation is mostly concentrated to the smallest resolved scales. Considering only fixed-coefficient standard finite difference filters, in the present study, it was found that the performance of the relaxation filtering method is very good, if the filter order m is sufficiently high, say $m \geq 8$. More precisely, optimal agreement between the DNS results and the LES results was found when using relaxation filters with order $8 \leq m \leq 10$. Furthermore, the study revealed that the performance of the relaxation filtering method is nearly independent of the filtering strength σ, provided that the filtering order m is sufficiently high, i.e., $m \geq 8$, and provided that the value of σ is not chosen unreasonably low, say $\sigma \geq 0.4$. Note that since the relaxation filtering frequency χ and the filtering strength σ have a similar influence on the results, the conclusions can be transfered to χ straightforwardly, i.e., the influence of the filtering frequency is almost negligible, for relaxation filters with sufficiently high order of accuracy.

In future work, a similar analysis will be done, taking into account the influence of the numerical discretization and de-aliasing. Using error landscapes, it is possible to quantify the interactions between modeling and numerical errors and to find optimal combinations of the filter order and the spatial discretization of the LES equations. It is obvious that the optimal error valleys of the relaxation filters, found in such a future study, will not necessarily be identical to those obtained in this work.

References

[1] P. Sagaut, *Large-Eddy Simulation for Incompressible Flows – An Introduction*, 3rd ed., Springer, Berlin/Heidelberg, 2005.

[2] B.J. Geurts, *Elements of Direct and Large-Eddy Simulation*, R.T. Edwards, Philadelphia PA, 2004.

[3] M. Lesieur and O. Métais, *New trends in large-eddy simulations of turbulence*, Annu. Rev. Fluid Mech. 28 (1996), pp. 45–82.

[4] F.F. Grinstein and C. Fureby, *Recent progress on MILES for high Reynolds number flows*, J. Fluid Eng. 124(4) (2002), pp. 848–861.

[5] J.A. Domaradzki, *Large eddy simulations without eddy viscosity models*, Int. J. Num. Meth. Fluids 24(10) (2010), pp. 435–447.

[6] J.A. Domaradzki and P.P. Yee, *The subgrid-scale estimation model for high Reynolds number turbulence*, Phys. Fluids 12(1) (2000), pp. 193–196.

[7] J.A. Domaradzki and N.A. Adams, *Direct modeling of subgrid scales of turbulence in large-eddy simulation*, J. Turbulence 3(24) (2002), pp. 1–19.

[8] J.A. Domaradzki, Z. Xiao, and P.K. Smolarkiewicz, *Effective eddy viscosities in implicit large eddy simulations of turbulent flows*, Phys. Fluids 15(12) (2003), pp. 3890–3893.

[9] C. Bogey and C. Bailly, *Decrease of the effective Reynolds number with eddy-viscosity subgrid-scale modeling*, AIAA J. 43(2) (2005), pp. 437–439.
[10] C. Bogey and C. Bailly, *Large eddy simulations of round jets using explicit filtering with/without dynamic Smagorinsky model*, Int. J. Heat Fluid Flow 27(4) (2006), pp. 603–610.
[11] T. Passot and A. Pouquet, *Hyperviscosity for compressible flows using spectral methods*, J. Comp. Phys. 75 (1998), pp. 300–313.
[12] G. Dantinne, H. Jeanmart, G.S. Winckelmans, V. Legat, and D. Carati, *Hyperviscosity and vorticity-based models for subgrid scale modeling*, Appl. Sci. Res. 59 (1998), pp. 409–420.
[13] S. Stolz, N.A. Adams, and L. Kleiser, *An approximate deconvolution model for large-eddy simulation of incompressible flows*, Phys. Fluids 13(4) (2001), pp. 997–1015.
[14] F. Ladeinde, X. Cai, M.R. Visbal, and D.V. Gaitonde, *Turbulence spectra characteristics of high order schemes for direct and large eddy simulation*, Appl. Numer. Math. 36(4) (2001), pp. 447–474.
[15] M.R. Visbal and D.P. Rizzetta, *Large-eddy simulation on curvilinear grids using compact differencing and filtering schemes*, J. Fluids Eng. 124(4) (2002), pp. 836–847.
[16] D.P. Rizzetta, M.R. Visbal, and G.A. Blaisdell, *A time-implicit high-order compact differencing and filtering scheme for large-eddy simulation*, Int. J. Num. Meth. Fluids 42(6) (2003), pp. 665–693.
[17] J. Mathew, R. Lechner, H. Foysi, J. Sesterhenn, and R. Friedrich, *An explicit filtering method for large eddy simulation of compressible flows*, Phys. Fluids 15(8) (2003), pp. 2279–2289.
[18] C. Bogey and C. Bailly, *Large eddy simulations of transitional round jets: Influence of the Reynolds number on flow development and energy dissipation*, Phys. Fluids 18(6) (2006), pp. 065101.
[19] C. Bogey and C. Bailly, *Turbulence and energy budget in a self-preserving round jet: Direct evaluation using large-eddy simulation*, J. Fluid Mech. 627 (2009), pp. 129–160.
[20] C. Bogey, O. Marsden, and C. Bailly, *Large-eddy simulation of the flow and acoustic fields of a Reynolds number* 10^5 *subsonic jet with tripped exit boundary layers*, Phys. Fluids 23(3) (2011), 035104.
[21] T. Tantikul and J.A. Domaradzki, *Large-eddy simulations using truncated Navier-Stokes equations with the automatic filtering criterion*, J. Turbulence 11(21) (2010), pp. 1–24.
[22] J. Berland, P. Lafon, F. Daude, F. Crouzet, C. Bogey, and C. Bailly, *Filter shape dependence and effective scale separation in large-eddy simulations based on relaxation filtering*, Computers & Fluids 47(1) (2011), pp. 65–74.
[23] G.I. Taylor and A.E. Green, *Mechanism of the production of small eddies from large ones*, Proc. R. Soc. A 158 (1937), pp. 499–521.
[24] M.E. Brachet, D.I. Meiron, S.A. Orszag, B.G. Nickel, R.H. Morf, and U. Frisch, *Small-scale structure of the Taylor-Green vortex*, J. Fluid Mech. 130 (1983), pp. 411–452.
[25] D. Fauconnier, C. De Langhe, and E. Dick, *Construction of explicit and implicit dynamic finite difference schemes and application to the large-eddy simulation of the Taylor-Green vortex*, J. Comput. Phys. 228 (2009), pp. 8053–8084.
[26] D. Drikakis, C. Fureby, F.F. Grinstein, and D. Youngs, *Simulation of transition and turbulence decay in the Taylor-Green vortex*, J. Turbulence 8(20) (2006), pp. 1–12.
[27] A.J. Chandy and S.H. Frankel, *Regularization-based sub-grid scale (SGS) models for large eddy simulations (LES) of high-Re decaying isotropic turbulence*, J. Turbulence 10(25) (2009), pp. 1–22.
[28] E. Johnsen, J. Larsson, A.V. Bhagatwala, W.H. Cabot, P. Moin, B.J. Olson, P.S. Rawat, S.K. Shankar, B. Sjögreen, H.C. Yee, X. Zhong, and S.K. Lele, *Assessment of high-resolution methods for numerical simulations of compressible turbulence with shock waves*, J. Comput. Phys. 229(4) (2010), pp. 1213–1237.
[29] N.A. Adams, *A stochastic extension of the approximate deconvolution model*, Phys. Fluids 23(6) (2011), 055103.
[30] G. Gregor and A. Beck, *On the accuracy of high-order discretizations for underresolved turbulence simulations*, Theoretical and Computational Fluid Dynamics, Springer Berlin/Heidelberg, 0935-4964, Physics and Astronomy, pp. 1–17.
[31] J. Meyers, B. Geurts, and P. Sagaut, *A computational error-assessment of central finite-volume discretizations in large-eddy simulation using a Smagorinsky model*, J. Comp. Phys. 227 (2007), pp. 156–173.

[32] C. Bogey and C. Bailly, *A family of low dispersive and low dissipative explicit schemes for flow and noise computations*, J. Comput. Phys. 194(1) (2004), pp. 194–214.
[33] J. Jeong and F. Hussain, *On the identification of a vortex*, J. Fluid Mech. 285 (1995), pp. 69–94.
[34] C.K.W. Tam, *Computational aeroacoustics – Issues and methods*, AIAA J. 33(10) (1995), pp. 1788–1796.
[35] C.K.W. Tam and K.A. Kurbatskii, *Multi-size-mesh multi-time-step dispersion-relation-preserving scheme for multiple-scales aeroacoustics problems*, Int. J. Comput. Fluid Dyn. 17(2) (2003), pp. 119–132.
[36] S.B. Muller, N.A. Adams, and L. Kleiser, *Analysis of relaxation regularization as subgrid-scale model for large-eddy simulation*, Proceedings of the fifth International ERCOFTAC Workshop on Direct and Large-Eddy Simulation, Munich, 2003.
[37] B. Vreman, B. Geurts, and H. Kuerten, *Comparison of numerical schemes in large-eddy simulation of the temporal mixing layer,* Int. J. Num. Meth. Fluids 22(4) (1996), pp. 297–311.
[38] J.P. Cholet and M. Lesieur, *Parameterization of small scales of three-dimensional isotropic turbulence utilizing spectral closures*, J. Atmos. Sci. 38 (1981), pp. 2747–2757.

Appendix A. Dissipation weighting coefficients

The filtering operation applied to a generic variable φ in Cartesian direction $i = 1, 2, 3$, using a standard finite difference filter, is defined by the convolution product

$$\widetilde{\varphi}(x_i) = \varphi(x_i) - \sum_{j=-n}^{n} d_j \varphi(x_{i,j}), \tag{A1}$$

where $\widetilde{\varphi}$ denotes the filtered variable, and $d_j = -d_{-j}$ represents the weighting coefficients that determine the dissipative contribution of the $(2n + 1)$-point standard symmetric filter with order $m = 2n$. The coefficients $d_{\pm j}$ are given in Table A1 for various filter orders m.

Appendix B. Influence of the filtering frequency

Figure B1 displays the energy spectrum, the kinetic energy, and the resolved dissipation rate for a fourth- and 10th-order relaxation filter with particular combinations of the filtering strength and the integer filtering interval θ (see Equation (14)). It is observed that doubling the filtering interval θ while keeping the strength σ constant appears to be equivalent to halving the filtering strength, while keeping θ constant. This means that the filtering frequency χ has a very similar influence on the results as the filtering strength σ. Although the effect of the frequency χ is significant for low-order filters, e.g., $m = 4$, the influence diminishes when increasing the filter order. For the 10th-order filter, the influence of χ is obviously very small, which confirms the findings of Stolz et al. [13].

Table A1. Weighting coefficients d_j of the dissipative contribution $\mathscr{D}(\mathbf{x})$ of standard symmetric finite difference filters $\mathscr{G}(\mathbf{x})$, with orders $m = 4, 6, 8, 10, 12,$ and 14.

m	$2n+1$	d_0	$d_{\pm1}$	$d_{\pm2}$	$d_{\pm3}$	$d_{\pm4}$	$d_{\pm5}$	$d_{\pm6}$	$d_{\pm7}$
4	5	3/8	−1/4	1/16	0	0	0	0	0
6	7	5/16	−15/64	3/32	−1/64	0	0	0	0
8	9	35/128	−7/32	7/64	−1/32	1/256	0	0	0
10	11	63/256	−105/512	15/128	−45/1024	5/512	−1/1024	0	0
12	13	231/1024	−99/512	495/4096	−55/1024	33/2048	−3/1024	1/4096	0
14	15	429/2048	−3003/16384	1001/8192	−1001/16384	91/4096	−91/16384	7/8192	−1/16384

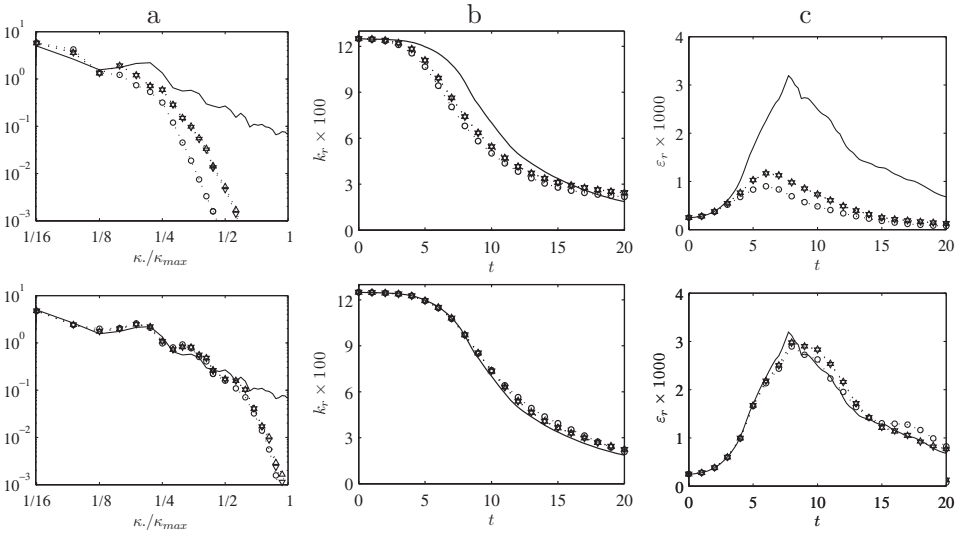

Figure B1. Energy spectra at $t = 9$ (a), evolution of kinetic energy filtered at $\kappa_c = 16$ (b), and evolution of resolved dissipation rate filtered at $\kappa_c = 16$ (c) for the ——— the 384^3 DNS, and the 64^3 LES using RF of order 4 (first row) and 10 (second row), with filtering strength $\sigma = 1.0$ and $\theta = 1$ (○), $\sigma = 1.0$ and $\theta = 2$ (△), and $\sigma = 0.5$ and $\theta = 1$ (▽).